Multiscale modeling and calibration framework for predicting the mechanical response of Li-ion battery cell components

Journal of Power Sources 659 (2025) 238237

Contents lists available at ScienceDirect

Journal of Power Sources

journal homepage: www.elsevier.com/locate/jpowsour

Multiscale modeling and calibration framework for predicting the mechanical response of Li-ion battery cell components

David Carlstedt [a,b,*], Amit Chetry [a,b], Carl Larsson [b], Ankeet Mohan Purantagi [a,b], Peter Gustavsson [a], Fredrik Larsson [b], Leif E. Asp [b]

[a] Battery Structural and Thermal Simulations, Volvo Car Corporation, SE-418 76 Gothenburg, Sweden
[b] Department of Industrial and Materials Science, Chalmers University of Technology, SE-412 96 Gothenburg, Sweden

GRAPHICAL ABSTRACT

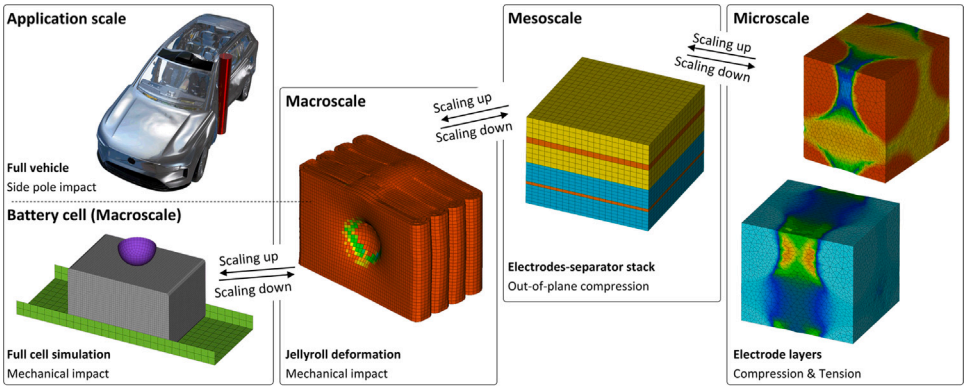

HIGHLIGHTS

- Framework to estimate mechanical properties across multiple length scales.
- Effective stiffness of binder-electrolyte and jellyroll modeled via homogenization.
- Mechanical impact tests performed on jellyroll sample and complete battery cell.
- Numerical predictions compared with experimental results.

ARTICLE INFO

Keywords:
Li-ion batteries
Electric vehicles
Finite element analysis
Model calibration
Homogenization

ABSTRACT

The mechanical response of battery cells plays a vital role in design of electric vehicles e.g., when evaluating their crashworthiness or studying the effects of cell swelling during operation. In this paper, we present a multiscale modeling framework for predicting the mechanical response of battery cell components at different length scales. Two design optimization loops for calibrating material model parameters are established. First, the effective mechanical response of the binder-conductive additive-electrolyte material phase inside the electrodes is estimated by performing homogenization of microscale Representative Volume Elements (RVEs), while utilizing experimental data for the effective electrode layer and data for the electrode particles from literature. Secondly, the effective response of the jellyroll is estimated by creating an RVE of the electrodes-separator stack and perform homogenization, while utilizing experimental data for the individual layers.

* Corresponding author at: Department of Industrial and Materials Science, Chalmers University of Technology, SE-412 96 Gothenburg, Sweden.
E-mail addresses: david.carlstedt@chalmers.se, david.carlstedt@ri.se (D. Carlstedt).

https://doi.org/10.1016/j.jpowsour.2025.238237
Received 28 May 2025; Received in revised form 23 July 2025; Accepted 24 August 2025
Available online 23 September 2025

Close agreement between numerical and experimental results are found for a jellyroll sample and a complete prismatic battery cell exposed to mechanical impact loading. By separating the length scales, and utilizing homogenization and calibration schemes, it is possible to estimate the mechanical response of the various material phases at the different length scales. This enables improved understanding of how battery cells behave under mechanical loads.

1. Introduction

The demand for electric vehicles (EVs) has increased in recent years with amplified restrictions on CO_2 emissions. In a foreseeable future, Li-ion batteries is the dominating solution for energy storage in EVs. In such application, the mechanical response of the battery cells plays an important role in the design of the battery pack. For example, it is a critical design parameter when evaluating the crashworthiness of the vehicle or when studying effects of cell swelling in a partly constrained environment during operation.

Battery cells come in different shapes and sizes, or so-called form factors (Fig. 1a). Moreover, the geometric features of the electrode configuration (or the so-called jellyroll) vary depending on the battery design (Fig. 1b–c). The relevant length scales for the jellyroll structure are: (i) Microscale (or layer level); (ii) Mesoscale (or stack level); (iii) Macroscale (or cell level), illustrated in Fig. 1d. The mechanical response of Li-ion batteries is known to be highly affected by a range of factors e.g., geometric features, material constituents and operating conditions (e.g., temperature) [1]. Additionally, the effective response depends on the mechanical loading conditions, or relative speed of the applied external mechanical force (due to its complex material composition being a combination of solid and liquid phases). Hence, given its complex geometric and microstructural configuration, estimating the mechanical response of Li-ion batteries becomes a non-trivial task involving several length and time scales.

In terms of EV application, two aspects have enforced this work: (i) Minimizing the risk for Internal Short-Circuit (ISC) caused by mechanical abuse [2,3]; (b) Estimating (and designing for) mechanical forces developed as a consequence of cell swelling, during operation [4–6]. It is noted that the aforementioned aspect is a highly complex phenomena which may lead to thermal events/runaway [3], and can originate from a variety of factors e.g., mechanical deformation (crushing or penetration), improper charging conditions (over-charge or over-discharge), or elevated temperatures, cf. Zhang et al. [7]. The relevant time scale for the load application associated with the two scenarios previously mentioned, deviate significantly. In terms of mechanical abuse during a crash event, the impact occurs over a very short time span (typically milliseconds). For the case of cell swelling on the other hand, the forces introduced by the constrained expansion of the cells evolve over the life time of the battery. For instance, Cao et al. [5] conducted cell swelling simulations using material data obtained from quasi-static experiments. Hence, the mechanical response of the cells during the two loading scenarios correspond to two different cases: dynamic (or high-velocity) impact, and quasi-static (or slow impact).

Over the last decade, several modeling approaches for estimating the mechanical response of Li-ion batteries have been proposed in the literature (see e.g. review papers on the subject [1,8]). Back in 2012 Sahraei et al. [9–11] proposed methods for estimating the mechanical response of Li-ion battery cells using homogenization, while attempting to predict failure associated with ISC due to mechanical impact loading. During the same time, Greve and Fehrenbach [12] established a macro-mechanical finite element (FE) based methodology to study crash simulation models for a cylindrical cell under quasi-static impact loading. In the work by Breitfuss et al. [13] the year after, all layers and their interactions were modeled for a pouch cell under quasi-static loading, and numerical and experimental results were compared. Since then, a lot of different modeling and experimental strategies have been proposed. For example, various cell form factors, e.g. cylindrical [14,15], prismatic [16,17], and pouch cells [18,19], have been studied in terms of their mechanical response. Moreover, different modeling strategies, accounting for operational conditions or mechanical loading rate have been proposed in the literature. For example, the effect of the state of charge (SOC) on the mechanical response of Li-ion batteries, accounting for the volume expansion of the cells, has been evaluated by Gilaki and Sahraei [20]. Moreover, Xu et al. [14] have developed a computational model of a 18 650 Li-ion battery with coupled strain rate and SOC dependencies. Additionally, modeling strategies relevant for battery stacks (for modules or packs level) have been proposed, see e.g. [4,21,22].

Various strategies for predicting ISC due to mechanical abuse have been proposed in the literature. For example, Chung et al. [18] studied failure of Li-ion batteries due to mechanical impact loading and proposed a Mohr–Coulomb based fracture criterion to predict failure (leading to ISC). Song et al. [23] recently proposed a more comprehensive ISC failure model entitled *the Sahraei Failure Criterion* which was developed from simulations of the microstructure of the electrodes-separator assembly.

Further, different experimental campaigns have been performed to study how Li-ion batteries respond to mechanical impact loading (recently also considering other battery cell chemistries e.g., Sodium-ion [24]). For example, Kalnaus et al. [25] have performed an experimental campaign (testing more than one hundred large format automotive pouch cells) under various impact velocities. Keshavarzi et al. [19] have performed in-situ characterization of material properties of pouch Li-ion batteries in tension from three-point bending tests. In terms of aged battery cells, Sprenger et al. [26] have studied the mechanical response of electrically cycled batteries from an EV battery module to investigate the influence of electrical aging and SOC on the mechanical and crash behavior of Li-ion batteries. Moreover, Jia et al. [27] have done a comprehensive review on the safety aspects of aged versus fresh battery cells exposed to mechanical abusive loadings. These experimental campaigns provide important understanding of the effective response of the cells. However, they lack information on how the various components and materials within the battery cell respond to the mechanical loads. To address this limitation, various papers have studied single component (or layer) properties of battery cells. For example, Cannarella et al. [28] have studied the mechanical properties of battery separators under compression and tension, and Gupta et al. [29] have measured how the mechanical (as well as certain electrical) properties of individual electrode layers are affected by electrochemical aging. Given the complexity of the length scales and material compositions involved, experimental testing to extract mechanical properties of the different materials inside battery cells becomes a highly non-trivial task. In particular, measuring mechanical properties of complex composite materials such as the binder-conductive additive-electrolyte phase poses significant difficulties. Iyer et al. [30] have measured mechanical properties of a polymer binder and the binder-particle interface using micromechanical testing. Even though these test methods are promising, they pose several challenges when it comes to e.g., estimate the effective response of binder-electrolyte composite inside the electrodes. Hence, virtual methods can provide a useful tool for assisting these experiments, identifying additional relations based on available data. Finally, even though a lot of work has been done within the field, there is still no consensus or standards for modeling or experimental procedures for evaluating the mechanical response of battery cells. For example, Zhu [31] has done an extensive review of various modeling techniques and mechanical testing procedures which

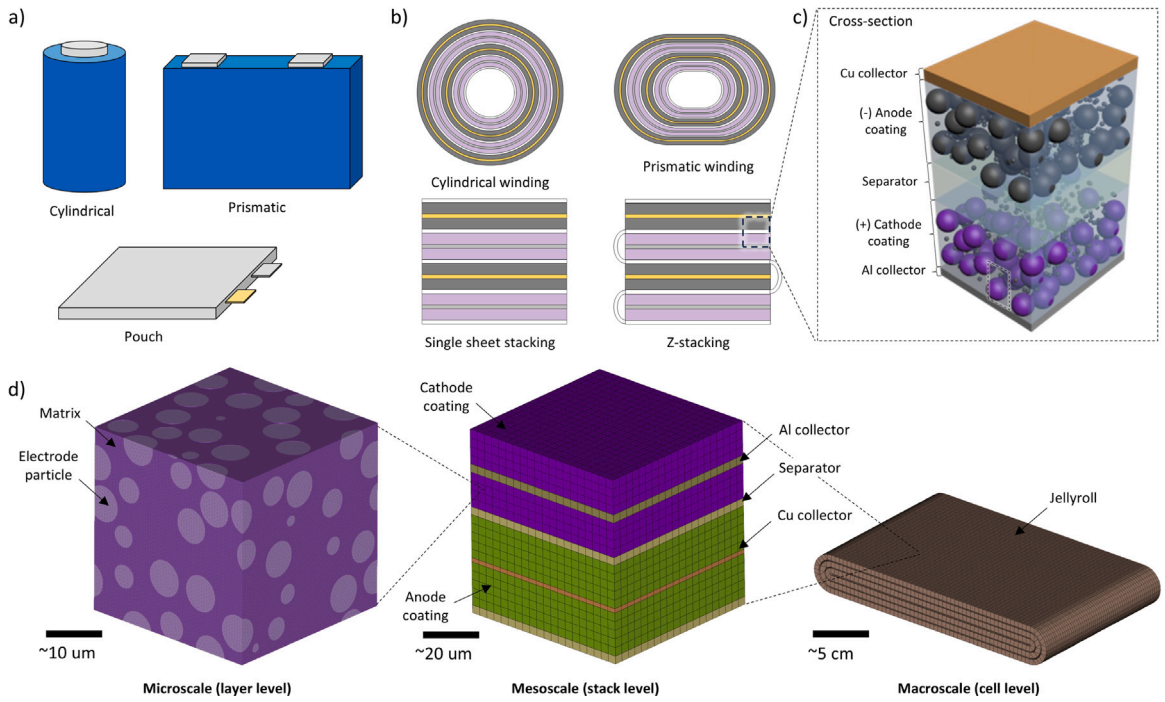

Fig. 1. (a) Examples of different battery form factors. (b) Different electrode configurations (jellyroll). (c) Cross-section of the electrodes-separator stack. (d) The studied length scales for the jellyroll structure. From left to right: (i) Microscale (or layer level); (ii) Mesoscale (or stack level); (iii) Macroscale (or cell level). The porous binder-conductive additive-electrolyte system at the microscale (here referred to as matrix), is treated as one medium with effective isotropic properties. At the mesoscale, all layers are treated as single-phase (homogeneous) mediums with effective properties, while effective (transversely isotropic) properties are assigned to the jellyroll at the macroscale.

revealed that although many methods exists, the results are often only valid in a narrow stress state, and thus cannot be used to validate one another.

For the transition between the meso- and macroscale (Fig. 1d), there are in general two different modeling approaches in the literature: (i) Detailed models, resolving each individual layer inside the battery cell; (ii) Homogenization strategies, estimating the effective response of the jellyroll utilizing Representative Volume Elements (RVEs). In terms of the former option, various authors have developed detailed models to simulate the mechanical response of battery cells under mechanical impact loading, see e.g., [15,32]. Spielbauer et al. [15] developed a discrete layered FE-model that can represent the internal stress and deformation of a battery cell. In this work, the authors also address various obstacles in material parameter measurements, meshing and convergence, and validation to enable future improvement of such models. Kulkarni et al. [33] have evaluated different FE modeling approaches including heterogeneous, homogeneous, hybrid and sandwich methods in terms of their suitability to simulate a real mechanical safety test procedures on battery cells under spherical indentation test on a sample pouch cell. Moreover, Sahraei et al. [16] have conducted a comprehensive study to estimate the mechanical response of Li ion prismatic battery cells, using a homogenization and failure calibration method. The same group has also developed a two-dimensional mesoscale-model (or RVE) of the cell stack and studied the sequence of failure in layers under complex loading scenarios [34]. Additionally, in-plane buckling and failure mechanism investigations have been performed using different RVEs, see e.g. [34,35]. Further, Gupta and Gudmundson [17,36] have developed a multiscale homogenization methodology that couples mechanics and electrochemistry on the meso- and macroscale. In these studies, RVEs for the electrodes-separator stack were used to process the transition between the layer/stack (mesoscale) and the battery cell level (macroscale).

In terms of the microstructural response, there are various studies and approaches for bridging the micro- and mesoscales (Fig. 1d). For example, Foster et al. [37] have developed a continuum mechanical model that resolves the individual active material particles of a Nickel Manganese Cobalt-oxide (NMC) cathode, and predicts the mechanical response of the cathode coating as a whole, with a detailed description of the electrode material configuration. Moreover, Ucel and Gudmundson [38] utilized a statistical RVE model for estimating effective mechanical properties and contact forces in battery electrode layers. Additionally, analytical and numerical methods have been proposed in the literature (see e.g. [39,40]) for estimating the effective stiffness of battery electrodes. Finally, various calibration schemes have been utilized or proposed in the literature. For example, Schmid et al. [41] recently proposed a calibration procedure based on a meta-model, while employing Proper Generalized Decomposition.

Modeling strategies proposed in the literature typically consider one scale transition. Moreover, analyses often rely on uncertain material data (e.g. the binder-conductive additive-electrolyte phase), which must be retrieved through complex experimental methods, cf. [30]. Furthermore, model calibration to estimate the effective response of the jellyroll inside the battery cell is often performed without proper initialization, ensuring a rational initial guess minimizing the risk for ending up with a non-physical calibrated material model (the risk increases significantly with increased complexity of the selected material model). Information on the execution and methodology behind said calibration routine is also often limited. To summarize, although extensive work has been done in the field to date, methods for systematically bridging all three (relevant) length scales: micro-, meso- and macroscale (utilizing homogenization and calibration schemes) to estimate the mechanical response of the various material phases (at the different scales), are lacking.

In this paper, we have developed a multiscale modeling framework for estimating the mechanical response of the material phases (at the different length scales) in Li-ion batteries by calibrating the macroscopic response in terms of its micro-structural properties. The model framework is set up at three length scales: (i) Microscale; (ii) Mesoscale;

(iii) Macroscale (Fig. 1d). Further, two design optimization loops for calibrating material model parameters are set up and performed. In the first design loop we back-calculate the effective response of the binder-conductive additive-electrolyte matrix by performing homogenization of microscale RVEs for the individual electrode layers, while utilizing experimental data for the electrode layer and the electrode particles (available in literature). As the second step, we create an RVE of the electrodes-separator stack and perform homogenization to retrieve the effective properties of the jellyroll of the cell. In both cases, the effective response is retrieved via homogenization, while calibration is used to estimate the model parameters for the selected constitutive models based on experimental data. By combining the different models, it is possible to move between length scales to identify unknown parameters or calibrate model parameters in a systematic manner. This framework also provides the basis for adding additional physical aspects in future work. A systematic framework for this purpose is to the authors' knowledge, not available in the literature to date.

2. Multiscale modeling scheme for the battery cell

In addition to the jellyroll, the battery cell contains several different components e.g., protective casing, terminals, support and protective structure like vents and gaskets, etc. In this work, we focus on the multiscale structure of the jellyroll. The cell casing is included in the macroscale model of the complete battery assembly (used for final validation) and is treated as homogeneous metal. Additional support structure such as tabs, terminals, and vent are not included for simplicity. Further, in the final validation step (simulating the complete battery cell), we study a prismatic cell design. It should be noted that the general formulation developed in this work is not limited to this particular form factor.

2.1. Multiscale jellyroll design

The jellyroll is often referred to as the (electrochemically) active part of the battery cell, as it facilitates the energy storage capability. The roll, or electrode stack, basically consists of a multilayered structure, comprising of two electrodes (cathode and anode), metallic current collectors (copper for anode and aluminium for cathode), and a porous separator layer, typically made from polymers (Fig. 1c). The electrode coatings and separator are porous structures saturated with a liquid electrolyte. Hence, multiple material phases are present at various length scales which showcase the complexity of estimating the structural response of the material with respect to mechanical loads. In this work, we study the multiscale structure of the jellyroll in terms of the three length (and modeling) scales illustrated in Fig. 1d.

2.1.1. Microscale

At the microscale, the complexity of varying scales and combination of materials are particularly relevant for the three phases: (i) the anode electrode coating layer, (ii) the cathode electrode coating layer, and (iii) the separator layer. The electrode coatings consist of electrode particles embedded in a porous polymer network (containing electron conductive additives), saturated with an (ion-conductive) liquid electrolyte. The saturated polymer system is here referred to as the binder-conductive additive-electrolyte matrix. The separator is highly porous and is typically made up by a polymer solid skeleton (e.g., polypropylene or polyethylene, often with a thin ceramic-based coating) saturated with liquid electrolyte. At the microscale, we treat the porous binder-conductive additive-electrolyte system as one medium with effective (matrix) properties. This simplification is motivated by the complexity of the binder system, and allows us to estimate an effective response of the matrix. Moreover, we treat the particles as a second (homogeneous) material phase in the electrode layers. The RVE for the electrode layers at this scale is shown in Fig. 1d. The RVE structures are generated as described in Section 3.2.1 RVE generation. For the separator, we treat the porous polymer network-electrolyte system a homogeneous (single-phase) medium with effective properties. Hence, no RVEs are created for the separator or the current collectors at this scale.

2.1.2. Mesoscale (electrodes-separator stack)

The mesoscale is modeled using an RVE of the electrodes-separator stack (Fig. 1d). The interfaces between the layers are treated as fully adhered i.e., the displacement field is continuous across the interfaces. This assumption is motivated by the fact that many battery designs to date utilize heat treatment to adhere the separator to the adjacent electrodes, enabling load transfer between the layers. At this scale, all layers are treated as homogeneous (single-phase) mediums with effective properties.

2.1.3. Macroscale (jellyroll)

The final level is the macroscale. This corresponds to the scale at which we assign effective properties of the jellyroll based on homogenization of the stack RVE at the mesoscale. We note that there are several modeling options at this scale e.g., the geometric representation of the jellyroll, element size and formulation, etc. In this paper, we study jellyrolls with prismatic winding electrode configuration and utilized the element size and split shown in Fig. 1d.

2.2. The three-scale problem

At each length scale we define, or select, a material model M_j^i for each constituent/layer as illustrated in Fig. 2a, where i denotes the length scale and j denotes the individual constituent (or material phase) at the corresponding scale. For each length scale, it is possible to input experimental test data (here referred to as $TEST$) which can be used to calibrate the model parameters for the individual constituents/layers or the effective properties of effective medium.

2.2.1. Quasi-static loading conditions

In this paper, we study the mechanical response under quasi-static loading conditions. We note that while these assumptions might be inaccurate in the case of dynamic (or high velocity) impact scenarios, this simplification is considered reasonable for many scenarios relevant for EV design. For example, such loading conditions are used for calibrating material response for battery cell swelling simulations (see e.g. [5]). In operational contexts, e.g., considering electrochemical–mechanical interactions under constrained cell swelling [42], the quasi-static response offers essential input for modeling how cells deform under slow, progressive loads. This supports multiphysics simulations that couple mechanical and electrochemical behavior (see e.g., [36,43]), enabling the interplay between mechanical constraints and electrochemical performance to be studied. Moreover, for early estimations of the mechanical response of batteries (in terms of mechanical impact loading) for battery pack designs and crashworthiness evaluation, the quasi-static loading scenario provides a favorable (repeatable) baseline for calibrating material model parameters before incorporating transient effects (strain-rate dependency). This baseline calibration ensures that any deviations observed under dynamic conditions are attributed to strain rate effects rather than inaccuracies in the base model as well as reduces the risk for overfitting [44].

3. Homogenization and calibration at the different length scales

In this section, we outline the homogenization and calibration schemes used to move between the length scales and calibrate model parameters for the selected constitutive models, respectively. In this study, we rely on the assumption of small strains. This choice is motivated by the computational cost of large scale models typically used in the EV design workflow. However, we allow for large deformations (separating deformation and rigid body displacements) by utilizing the co-rotational element formulations in the commercial software LS-Dyna. Specifically, the co-rotational formulation is used for the shell elements in the models, for which the total nodal motion is split into a large rigid body translation and a rotation. The small local deformation of the element is evaluated in a co-rotational frame, enabling linearized

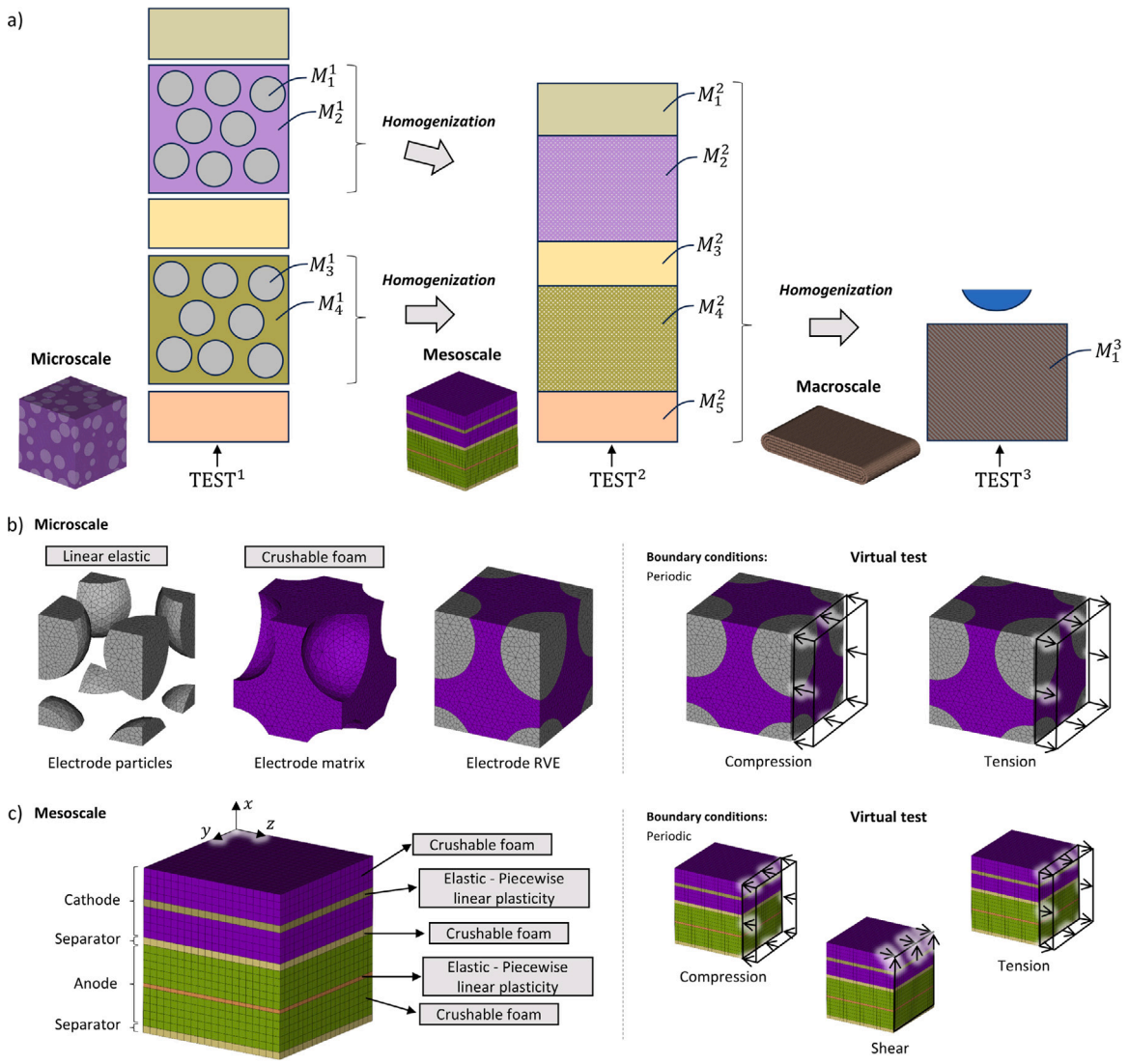

Fig. 2. (a) The material models are denoted M_j^i, where i and j denotes the length scale and constituent at the corresponding scale, respectively. Experimental test data are referred to as $TEST$ and can be input at each length scale. Homogenization is used to derive the effective properties for the heterogeneous medium, allowing us to move between the length scales (illustrated with the arrows). Material models and load cases used for the virtual testing: (b) Microscale (particle-electrode matrix) RVE; (c) Mesoscale (electrodes-separator stack) RVE. For the mesoscale, six load cases are simulated (transversely isotropic response). The x-axis is defined in the out-of-plane direction, while the y–z plane corresponds to in-plane.

strain computation with lower computational cost and enhanced stability. In LS-Dyna, the co-rotating frame updates every timestep, evaluate local element stiffness and forces in the local frame, and transform them back to global coordinates. This enables accurate and stable modeling of large rigid motions with moderate local deformations, making them especially effective for predicting complex crash behavior like buckling or folding of thin-walled structures. For the solid elements, the large deformations are instead handled using a fully nonlinear updated Lagrangian formulation without motion decomposition. For both the implicit and explicit analysis, we use fully integrated 8 nodal hexahedral solid elements (intended for poor aspect ratios and referenced as ELFORM = −2 in the LS-Dyna manual [45]) which alleviate transverse shear locking by modifying the jacobian matrix in such a way that the spurious stiffness is reduced [46]. This allows the solids to capture severe distortions or crushing. Hence, this combination of elements is therefore well suited for computationally efficient large scale crash or impact simulation models, where large deformations are expected. For more information on the implementation of these elements, we refer to the LS-Dyna manual [45].

3.1. Homogenization

Homogenization (or virtual testing) is used to replace the heterogeneous medium with an equivalent homogeneous one. The goal is to derive the effective properties for a heterogeneous medium that allow bridging between the different length scales (cf. Fig. 2a).

In terms of mechanical response, the microscopic stress must satisfy the equilibrium equation (balance of linear momentum) in the RVE, which in the absence of body forces, is defined as

$$-\boldsymbol{\sigma} \cdot \nabla = 0 \tag{1}$$

where $\boldsymbol{\sigma}$ is the (small strain) stress tensor at the heterogeneous scale. The stress–strain relation (or constitutive model) at the microscale is defined as

$$\boldsymbol{\sigma} = \boldsymbol{\sigma}(\boldsymbol{\varepsilon}, \boldsymbol{q}) \tag{2}$$

where $\boldsymbol{\varepsilon} = \frac{1}{2}[\mathbf{u} \otimes \nabla]^{\text{sym}}$ is the (microscopic) strain tensor (defined in terms of the displacement field $\mathbf{u}$), and $\boldsymbol{q}$ denotes a set of internal variables such as, e.g., inelastic strains or hardening variables, that need

to be solved from accompanying constitutive evolution models. The effective macroscopic stress $\bar{\sigma}$ and strain $\bar{\varepsilon}$ are derived as the volume averages of their microscopic counterparts[1]

$$\bar{\boldsymbol{\sigma}} = \langle \boldsymbol{\sigma} \rangle = \frac{1}{|\Omega_{\square}|} \int_{\Omega_{\square}} \boldsymbol{\sigma} \, \mathrm{d}\Omega \tag{3}$$

$$\bar{\boldsymbol{\varepsilon}} = \langle \boldsymbol{\varepsilon} \rangle = \frac{1}{|\Omega_{\square}|} \int_{\Omega_{\square}} \boldsymbol{\varepsilon} \, \mathrm{d}\Omega \tag{4}$$

where $\langle \cdot \rangle$ denotes the volume average and $\Omega_{\square}$ denotes the RVE volume. The stress–strain relation at the macroscale can now be defined as

$$\bar{\boldsymbol{\sigma}} = \bar{\boldsymbol{\sigma}}(\bar{\boldsymbol{\varepsilon}}) \tag{5}$$

which is implicit in the sense that its evaluation requires the solution of a boundary value problem on the RVE. In the special case of linear elasticity, the microscale constitutive model and the corresponding macroscale (effective) model reads

$$\text{Microscale: } \boldsymbol{\sigma} = \mathbb{E} : \boldsymbol{\varepsilon}, \quad \text{Macroscale: } \bar{\boldsymbol{\sigma}} = \bar{\mathbb{E}} : \bar{\boldsymbol{\varepsilon}} \tag{6}$$

where $\mathbb{E}$ and $\bar{\mathbb{E}}$ are the fourth-order stiffness tensor at the microscale and (the corresponding effective counterpart) at the macroscale, respectively. The coefficients in $\bar{\mathbb{E}}$ can be determined by solving for six unit strain load cases on the RVE, see [47]. In this work, we seek to move between the involved length scales by deriving, or back-calculating, material model coefficients representing these relations.

3.2. Representative Volume Element (RVE)

The RVE is used to estimate effective/representative values of the physical properties for the larger domain. In this study, we utilize two RVEs at the length scales: micro- and mesoscale, shown in Fig. 2. Periodic boundary conditions are used for the microscale and mesoscale RVEs, using the built-in RVE tool in LS-Dyna (Keyword: *RVE_ANALYSIS_FEM [48]). To estimate the effective quantities in Eqs. (3) and (4) (in terms of the assumed properties of the microscale phases) a set of deformation modes, representing the various strain states, are applied (cf. Fig. 2b–c).

3.2.1. RVE generation

Two types of RVE structures are generated at the two length scales: micro- and mesoscale. At the microscale, the RVE structures (representing the electrode layers) are generated using the *RVE generation tool* available in the commercial software ANSA pre-processor. The RVE corresponds to a cube with equal side lengths (l_{RVE}). This length is first defined, followed by setting the particle inclusion radius (r_{p}) and its aspect ratio (circular), as well as parameters related to the inclusion generator (e.g. minimum distance between inclusions, maximum number iterations, etc.). It is possible to generate inclusions with various sizes and shapes. For simplicity, same size circular inclusions are used in this study. The material model parameters are assigned to the phases once the RVE is generated. To enable periodic boundary conditions, periodicity is enforced by adding constrains to the RVE generator on conformable mesh. It is worth noting that the RVE generator also asks for target mesh size (chosen to accurately resolve the particle-matrix geometry) and outputs a meshed geometry with tetrahedral solid elements. Due to known limitations of tetrahedral elements in large deformation problems, we split the tetrahedral elements into hexahedral elements after the RVE is generated (with a built in function in ANSA). At the mesoscale, the RVE structures (representing the electrode stacks) are generated by creating cubes with equal side lengths, corresponding to the total thickness of the electrode stack. The cube is then split into segments, representing the different layers (electrodes, separator, collectors), and meshed with hexahedral solid elements. Finally, we note that the selected RVEs at the microscale represent a perfectly periodic microstructure. If we were to model a specific material, the statistical representation (particle size distribution, clustering, etc.) would affect the required RVE size. At the mesoscale, the RVE can be considered perfectly period in the through thickness direction and the response is insensitive to the in-plane RVE size.

[1] We note that appropriate boundary conditions must be applied at the RVE level for Eq. (4) to hold.

3.3. Material model: Elasto-plastic (small strain setting)

The material models used for the various constituents and components (at the different length scales) are listed in Table 1. We note that the model parameters are either based on data from the literature directly (e.g. properties for the anode and cathode particles) or estimated/calibrated based on experimental data (e.g. anode and cathode coating layers). The utilized constitutive models are: Linear elastic (*MAT_001); Elastic-Piecewise linear plasticity (*MAT_024), Uncoupled crushable foam (*MAT_063), and Transversely isotropic crushable foam (*MAT_142), where *MAT refers to the specific material card in the LS-Dyna library [49]. The material model is linked to the assumed constitutive relation between the stress and strain.

The constitutive relation for the linear elastic material model (*MAT_001) is defined according to the well known Hooke's law, cf. Eq. (6) for the microscale problem. In Eq. (6), $\mathbb{E}$ is the fourth-order elasticity tensor, typically expressed in terms of Young's modulus E and Poisson's ratio ν for isotropic materials. In the case of anisotropic response, the elasticity tensor is described in terms of its directional properties. From mechanical testing on battery cell components (under various loading conditions), see e.g. [15,16], it is clear that the stress–strain relation is non-linear already for small strains. To capture such behavior within the regime of small strain settings, a simple option is to use elasto-plastic models. To introduce plasticity for small strains, the strain tensor is additively decomposed into elastic and plastic parts

$$\boldsymbol{\varepsilon} = \boldsymbol{\varepsilon}^{\mathrm{e}} + \boldsymbol{\varepsilon}^{\mathrm{p}}. \tag{7}$$

The constitutive (material) relation can now be expressed as

$$\boldsymbol{\sigma} = \mathbb{E} : [\boldsymbol{\varepsilon} - \boldsymbol{\varepsilon}^{\mathrm{p}}]. \tag{8}$$

Next, a yield criterion in terms of yield stress σ_y and a hardening behavior is introduced. For the utilized Elastic-Piecewise linear plasticity model in LS-Dyna (*MAT_024), the yield function is based on the von Mises stress

$$f(\boldsymbol{\sigma}) = \sigma_{\mathrm{eq}} - \sigma_y(\bar{\epsilon}^p) \tag{9}$$

where $\sigma_{\mathrm{eq}} = \sqrt{\frac{3}{2}\boldsymbol{s} : \boldsymbol{s}}$ is the equivalent von Mises stress, for $\boldsymbol{s} = \boldsymbol{\sigma} - \frac{1}{3}\mathrm{tr}(\boldsymbol{\sigma})\boldsymbol{I}$ being the deviatoric stress tensor, and $\bar{\epsilon}^p = \int_0^t \sqrt{\frac{2}{3}\dot{\boldsymbol{\epsilon}}^p : \dot{\boldsymbol{\epsilon}}^p}\, \mathrm{d}t$ is the equivalent plastic strain, defined in terms of the plastic strain rate $\dot{\boldsymbol{\epsilon}}^p$. Thereby, we assume isotropic hardening. Moreover, $\sigma_y(\bar{\epsilon}^p)$ is a piecewise linear function discretized at $\sigma_y(\bar{\epsilon}^p_n)$ for $n = 0, 1, 2, \ldots$. The plastic response is basically defined in terms of parametric points of $[\sigma_y(\bar{\epsilon}^p_n), \bar{\epsilon}^p_n]$, corresponding to the equivalent plastic strain versus yield stress (handled as a *Load curve* in LS-Dyna). The behavior is the same for compression and tension.

In terms of the crushable foam model (*MAT_63), the plasticity relation is modified to account for the highly compressible behavior typical of foams. During compression the foam compacts which leads to a rapid increase in stiffness with high volumetric stain. To capture this behavior, a nonlinear relationship between hydrostatic stress and volumetric strain is introduced. Compared with the Piecewise linear plastic model, we introduce a hydrostatic pressure dependent yield function defined as

$$f(\boldsymbol{\sigma}) = p - p_y(\varepsilon_v) \tag{10}$$

where $p = \frac{1}{3}\mathrm{tr}(\boldsymbol{\sigma})$ is the mean (hydrostatic) stress, $p_y(\varepsilon_v)$ is the yield function defining the yield surface in terms of volumetric strain $\varepsilon_v =$

Table 1
List of material models used for the various components, at the different length scales. The material parameters for the Binder-conductive additive(CA)-Electrolyte matrix (microscale) and the jellyroll (macroscale) are considered unknown and are identified via combining homogenization and calibration.

Material	Length scale	Material model	Calibrated	Reference
Cathode particle (M_1^1)	Micro	Linear elastic (*MAT_001)	No	[50]
Anode particle (M_3^1)	Micro	Linear elastic (*MAT_001)	No	[50]
Binder-CA-Electrolyte (M_2^1, M_4^1)	Micro	Uncoupled crushable foam (*MAT_063)	Yes	–
Al collector (M_1^2)	Meso	Piecewise linear plasticity (*MAT_024)	Yes	[15]
Cathode coating layer (M_2^2)	Meso	Uncoupled crushable foam (*MAT_063)	Yes	[15]
Separator layer (M_3^2)	Meso	Uncoupled crushable foam (*MAT_063)	Yes	[15]
Anode coating layer (M_4^2)	Meso	Uncoupled crushable foam (*MAT_063)	Yes	[15]
Cu collector (M_5^2)	Meso	Piecewise linear plasticity (*MAT_024)	Yes	[15]
Jellyroll (M_1^3)	Macro	Transversely isotropic crushable foam (*MAT_142)	Yes	–
Casing	Macro	Piecewise linear plasticity (*MAT_024)	No	–

tr(ε). For this model, the hardening rule is defined in terms of $p_y(\varepsilon_v)$. In this study, we apply the corresponding (parametrized) piecewise linear function in terms of parametric points of $[p_y(\varepsilon_{v,n}), \varepsilon_{v,n}]$, corresponding to the volumetric strain versus yield stress. Unloading is fully elastic and in tension, the behavior is treated as elastic-perfectly-plastic with the transition denoted as the tensile stress cutoff (σ^T).

3.4. Calibration

To calibrate the parameters of the constitutive models M_j^i in terms of relevant experimental test data *TEST*, two design optimization loops are set up in the commercial software LS-OPT [51] (Fig. 3).

For *design optimization loop* 1, we calibrate the parameters of the constitutive model for the binder-conductive additive-electrolyte matrix (M_2^1, M_4^1) by performing virtual testing on the microscale RVE (homogenization) and compare the computed response versus experimental data for the electrode layer (mesoscale). In this loop, we assume that the properties of the electrode particles are known and utilize experimental data from the literature for these constituents [50].

For *design optimization loop* 2, we calibrate the parameters of the constitutive model for the jellyroll (M_1^3). The optimization loop consists of two steps. The first step corresponds to the *initialization* step. To get an initial guess for the effective properties of the jellyroll, prior to the final calibration, we utilize the mesoscale RVE of the electrodes-separator stack. We start by calibrating the parameters for the constitutive models of the individual layers (M_j^2) versus experimental data at the corresponding scale. Once the parameters are identified, we perform homogenization to retrieve the effective properties of the jellyroll based on the mesoscale RVE. Next, we perform the *final calibration* step, where we calibrate the model parameters for the jellyroll using the impact simulation model. As initial guess to the calibration loop, we utilize the estimated parameters for the jellyroll from the RVE simulations. The impact simulation model is then imported to the calibration framework in LS-OPT ([51]) together with experimental data (of measured impactor displacement and force exerted on the impactor). We can now execute the calibration loop to identify material model parameters of the jellyroll for which the numerical and experimental estimates of the force versus displacement of the impactor are as similar as possible.

In terms of the optimization routine, the design variables are the n unknown model parameters for the evaluated constitutive models denoted as $\boldsymbol{\psi} = [\psi_1, \psi_2, \dots, \psi_n]$. Further, design constraints are placed on the design variables $\boldsymbol{\psi}$ to limit the design space. The correlation is done by ordinate-based curve matching using the Mean Square Error (MSE) of the difference between the computed effective macroscopic stress–strain data ($\bar{\sigma}$, $\bar{\varepsilon}$) and the imported (corresponding) test data curve. The optimization problem is defined as follows

$$\min \left(\frac{1}{N} \sum_{n=1}^{N} W_n \left(\frac{g_n(\boldsymbol{\psi}) - G_n}{s_n} \right)^2 \right) \tag{11}$$

In Eq. (11), $g_n(\boldsymbol{\psi})$ is the simulated response at $\bar{\varepsilon}_n$ for given parameters ψ, and G_n corresponds to the experimental value at point $\bar{\varepsilon}_n$, N is the total number of points (where the MSE is computed), and W_n and s_n are the weights (applied to the squared error) and scaling factor, respectively. Hence, we seek to identify the unknown model parameters $\boldsymbol{\psi}$ which minimize the given objective function (within the considered design space). The optimization is performed utilizing a linear polynomial response surface (with D-Optimal point selection) in accordance with the Sequential Response Surface Method (SRSM) available in the LS-OPT suite [51].

4. Results and discussion

4.1. The micro- to mesoscale problem

We start by simulating the RVE problem at the microscale (Fig. 4a). For these simulations, the implicit solver in LS-Dyna is used [45]. Model parameters used as input for the microscale RVE model are summarized in Table 2. The output of the RVE model from the simulated RVE load cases are the average stress–strain response of the particle-matrix composite in the different directions. The evaluated load cases are uniform compression and tension (displacement applied along one side, while periodic boundary conditions are used for the remaining faces). These load cases are assumed to correspond to the loading conditions for the imported experimental data (from [15,52]) shown in Fig. 4b. The properties of the particles are assumed to be known linear elastic and are based on the work by Qi et al. [50], listed in Table 3. Further, the volume fractions of particles in the two electrodes are assumed to be 0.33, for simplicity. We note that commercial electrodes typically have particles of varying size and volume fractions. However, in this work we simplify to same-size particles. The anode and cathode particles are assumed to be graphite and Lithium Cobalt Oxide (LCO), respectively. For the effective response of the anode and cathode coating layers we utilize experimental data from the work by Speilbauer et al. [15] and Ji et al. [52], respectively (shown in Fig. 4b). In terms of material model for the matrix, we use the Uncoupled crushable foam (*MAT_063) and assume a Poisson's ratio of 0.01 (Table 3). The unknown design variables (ψ_i) for the calibration loop correspond to the remaining model parameters for the matrix: E_m, σ_m^T, and the hardening curve

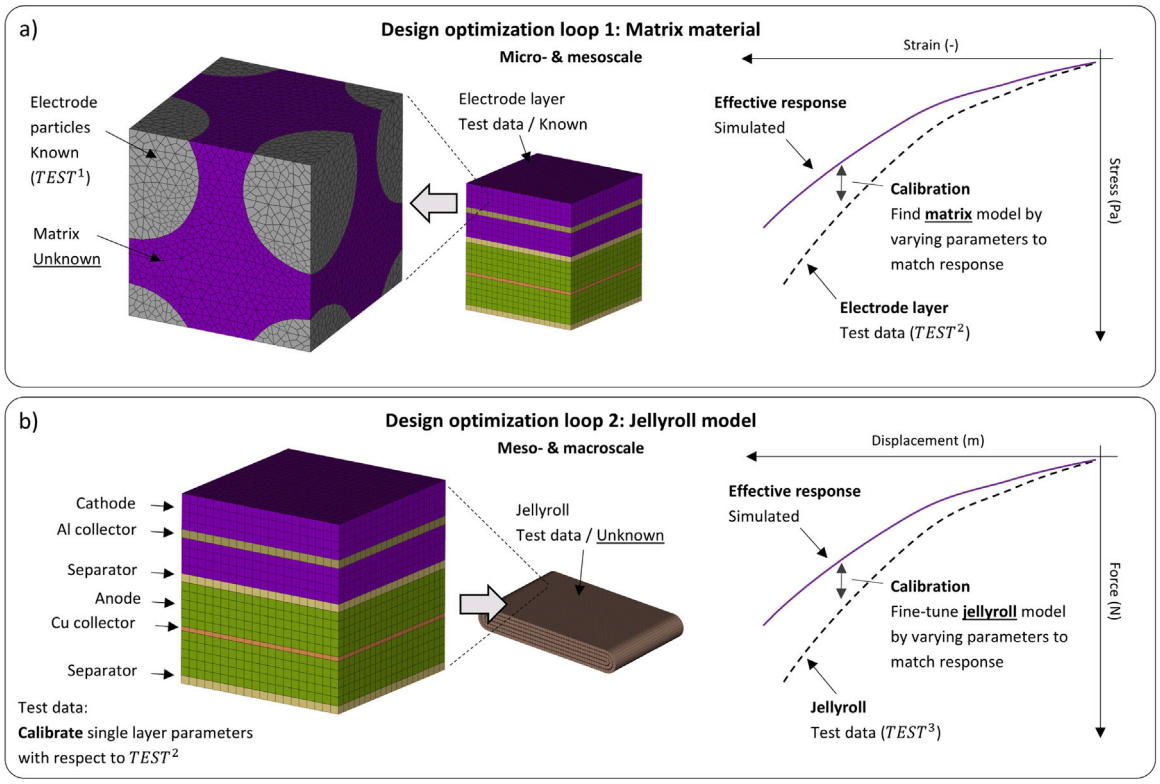

Fig. 3. Calibration procedures to estimate parameters of the constitutive models M_j^i in terms on relevant experimental test data *TEST*. (a) Design optimization loop 1: Calibrate the material model parameters of the binder-conductive additive-electrolyte matrix (micro- and mesoscale). (b) Design optimization loop 2: Calibrate the material model parameters of the individual layers and perform homogenization to retrieve the effective properties of the jellyroll (meso- and macroscale).

$p_{y,m}(\varepsilon_v)$ (cf. Table 2). The hardening curve is defined in terms of four predefined volumetric strain levels: $\varepsilon_v = 0, -0.05, -0.1, -0.15$, for which we seek the corresponding yield stress values: $p_{y,m}(\varepsilon_v = 0)$, $p_{y,m}(\varepsilon_v = -0.05)$, $p_{y,m}(\varepsilon_v = -0.1)$, $p_{y,m}(\varepsilon_v = -0.15)$. Additional information on the utilized design space for the model parameters is provided in Appendix A. In Fig. 4c, the effective stress ($\bar{\sigma}$) as function of the effective strain ($\bar{\varepsilon}$) for the final iteration (optimized solution) are plotted together with the test data (from [15,52]) for the anode and cathode, respectively. The simulated load cases correspond to uniform compression and tension. The effective strain field at a number of time increments during the simulation (t_i^S) for the anode are shown for illustrating the corresponding deformation modes. The calibrated material parameters for the matrix system for the anode and cathode are presented in Fig. 4d–e.

From Fig. 4c it can be seen that the numerical and experimental results demonstrate the following behavior: (i) Both electrodes behave similar in tension (mode governed by the matrix); (ii) The response in compression is noticeably different for large compression (mode governed by the particle-matrix combination). Firstly, we note that the properties of the matrix are similar for the two electrodes (as expected), cf. Fig. 4d–e. The main difference between the two constitutive models is the behavior for large compression (Fig. 4e). This difference is assumed to be associated with the simplistic representation of the electrodes in combination with the utilized test data. Since the samples are tested in virgin state, the anode particles corresponds to graphite (C) without any lithium ($E_p^{\text{ano}} = 32$ GPa) and for the cathode corresponds to the lithiated state LCO, or $LiCoO_2$ ($E_p^{\text{cat}} = 264$ GPa), cf. [50]. The difference in compressive behavior is assumed to be linked to the different stiffness of the particles in combination with particle volume fraction. Further, it should be noted that experimental data for electrode layers vary noticeably between sources and test setups. Hence, with more detailed description of the RVEs, in combination with more reliable experimental data, it will be possible to retrieve better estimates of the effective response of the matrix (utilizing the proposed methodology).

Iyer et al. [30] have performed micromechanical testing, including micropillar compression, microcantilever bending, and nanoindentation, to measure the mechanical properties of the polymer binder phase in battery electrode layers. In this study, only the binder phase was evaluated and the experimental results from this study showed a stiffer response as compared to the estimated properties of the binder-conductive additive-electrolyte matrix (cf. Fig. 4d–e). Upon the assumption that the liquid electrolyte provides limited stiffness in the case of quasi-static loading, the stiffness of the binder-electrolyte composite is expected to be lower. Hence, the estimated response (Fig. 4d–e) is qualitatively in agreement with the reported measurements in [30].

The particle volume fraction of the RVE is of high importance for the effective stiffness of the electrode. The shape of individual particles on the other hand, is considered less important for the effective stiffness, but critical when attempting to resolve local stress fields at electrode–electrolyte interfaces. In Fig. 5a, the effective stress ($\bar{\sigma}$) as function of the effective strain ($\bar{\varepsilon}$) are shown for different volume fraction of particles (V_p) for the compression load case of the calibrated anode RVE. The results clearly show that increased V_p results in increased compressive stiffness of the medium. Hence, it is important to know the correct volume fractions to ensure reliable estimates of the matrix response. In Fig. 5b, the effective stress as function of the effective strain are shown for different RVE sizes/dimensions. The RVE size is defined relative to the particle radius. The smallest RVE (with a cubic side length of $l_{\text{RVE}} = 3.33\, r_p$, where r_p is the particle radius) corresponds to the one utilized in the calibration loop earlier. It should be noted that the RVE size is changed by generating new RVEs. This means that small difference will be present due to the rearrangement of the particles. These results indicate that the selected dimensions of the original RVE are large enough to be representative for capturing the overall response.

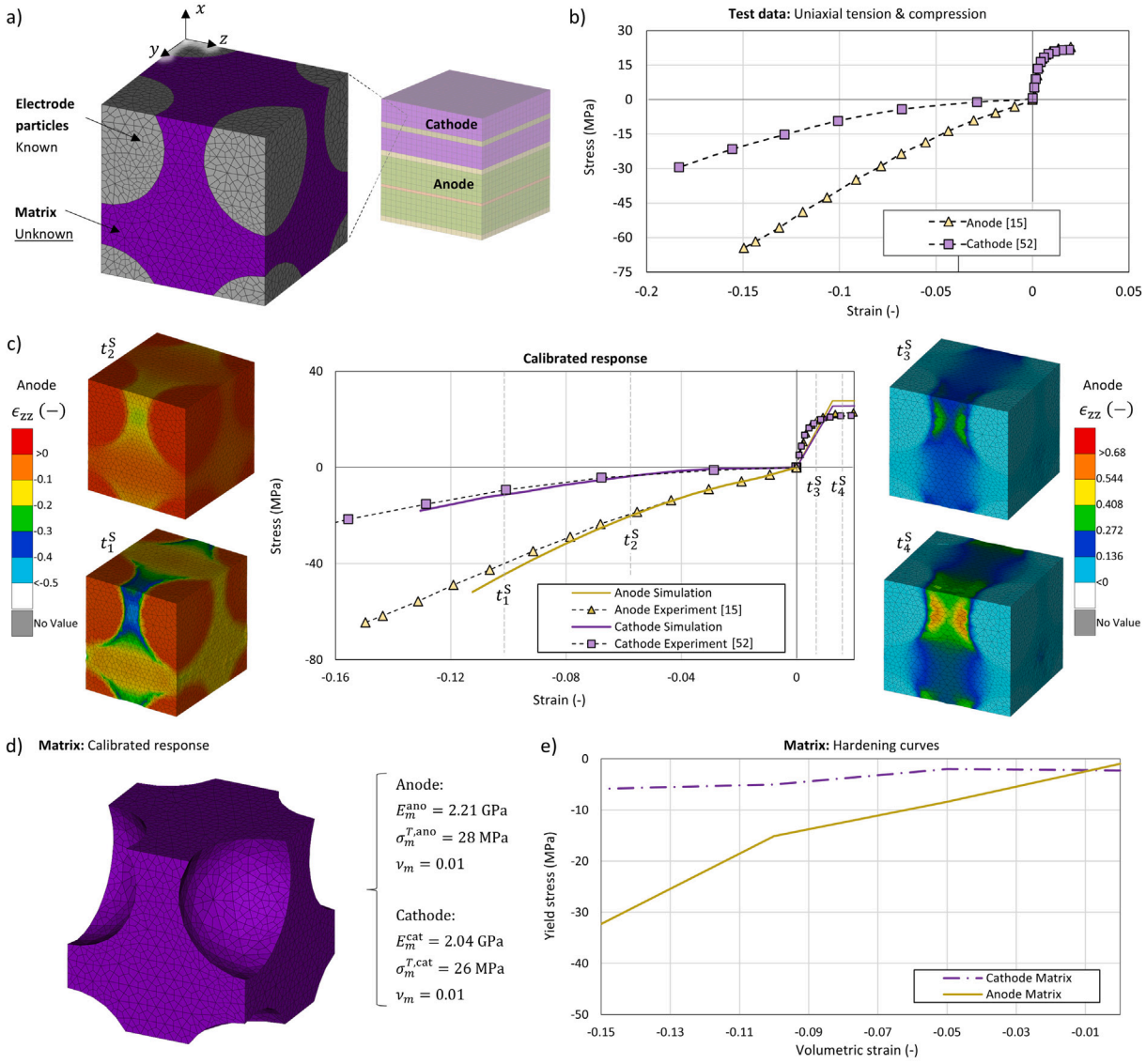

Fig. 4. Micro- and mesoscale. Design loop 1: Matrix material calibration. (a) The unknown material response is the binder-conductive additive-electrolyte matrix. (b) Experimental data for the anode and cathode electrode layers are imported from [15] and [52], respectively. (c) The effective stress ($\bar{\sigma}$) as function of the effective strain ($\bar{\epsilon}$) for the final iteration (optimized solution) together with the test data (from [15,52]) for the anode and cathode, respectively. The strain fields (ϵ_{zz}) for the anode at a number of time instances (t_i^S) are also shown to illustrate the modes of deformation. (d) Calibrated material parameters for the matrix system for the anode and cathode. (e) Estimated hardening curves utilizing a piecewise linear approximation with 4-points for the two matrix systems.

4.2. The meso- to macroscale problem

The second scale transition is the meso- to macroscale problem. For this scale transition we study two cases: (i) Small scale sample of a jellyroll (without liquid electrolyte), and (ii) full scale battery cell of prismatic format (with aluminium casing and liquid electrolyte). The two cases are presented in the following.

4.2.1. Small scale jellyroll sample

The small scale jellyroll sample was manufactured manually by assembling a electrodes-separator stack of dimensions 70 by 70 mm. The total thickness of the sample was 1.82 mm, corresponding to 8 repeatable units (or RVEs) in the thickness direction. Model parameters used as input for the mesoscale RVE model and the impact simulation model for the small scale jellyroll sample are provided in Table 4. We now consider homogenization from the mesoscale representative unit (RVE) to the effective jellyroll model, cf. Section 3.1. The stack design for the small scale sample (or mesoscale RVE) is shown in Fig. 6a and the geometric model parameters for the RVE are summarized in Table 5.

For this problem, we start by importing experimental data for the effective response of the individual layers from [15] (show in Fig. 6b). It should be noted that the cathode material is now assumed to be NMC and the corresponding test data which is used, exhibit a noticeable stiffer response in compression (compared to the LCO electrode in [52]). Moreover, for the separator we assume isotropic response (for simplicity) and use properties for the machine direction. Based on this input, we calibrated the elastic modulus and tensile stress cutoff or yield stress for the respective layers within the electrodes-separator stack RVE (in terms of the selected constitutive models). For the hardening curves of each layer, we import the experimental data directly as *Load curves*. The estimated parameters are summarized in Table 4. Next, we simulate the virtual load case of uniform compression, tension and shear for the in-plane and out-of-plane cases (i.e. 6 load cases) to retrieve the effective response in terms of transverse isotropy for the stack (Fig. 6c). The estimated model parameters for the jellyroll (based

Table 2
Summary of model parameters used as input for the microscale RVE. The output from the RVE simulations are the average stress and strain fields of the particle-matrix composite. Parameters marked as "Calibrated" correspond to design variables in the calibration loop (calibrated values are reported in the table, while initial values and design space used in the calibration are found in Appendix A). Parameters marked as "Fixed", are fixed values.

Input	Parameter	Definition	Data type	Output
Geometry: RVE	RVE side length	l_{RVE} = 21 μm	Fixed	Stress–strain response
	Particle radius	r_{p} = 6 μm	Fixed	
	Solid elements (8 nodal hexahedral)	35 444	Fixed	
	Approximate element size	0.5 μm	Fixed	
Material: Particle	Elastic modulus	See Table 3	Fixed	
	Poisson's ratio	See Table 3	Fixed	
Material: Matrix anode	Elastic modulus (tension)	E_m^{ano} = 2.21 GPa	Calibrated	
	Poisson's ratio	See Table 3	Fixed	
	Tensile stress cutoff	$\sigma_m^{T,\mathrm{ano}}$ = 28 MPa	Calibrated	
	Hardening curve	$p_{y,m}^{\mathrm{ano}}(\varepsilon_v)$, Fig. 4e	Calibrated	
Material: Matrix cathode	Elastic modulus (tension)	E_m^{cat} = 2.04 GPa	Calibrated	
	Poisson's ratio	See Table 3	Fixed	
	Tensile stress cutoff	$\sigma_m^{T,\mathrm{cat}}$ = 26 MPa	Calibrated	
	Hardening curve	$p_{y,m}^{\mathrm{cat}}(\varepsilon_v)$, Fig. 4e	Calibrated	

Table 3
Adopted material properties. Anode: Graphite, Cathode: Lithium Cobalt Oxide (LCO). Model parameters for the binder-conductive additive-electrolyte matrix system are estimated via calibration.

Material	Volume fraction [–]	Elastic modulus [GPa]	Poisson's ratio [–]	Reference
Anode particle: Graphite	0.33	32	0.32	[50]
Cathode particle: LCO	0.33	264	0.32	[50]
Binder-conductive additive-electrolyte	0.66	–	0.01	–

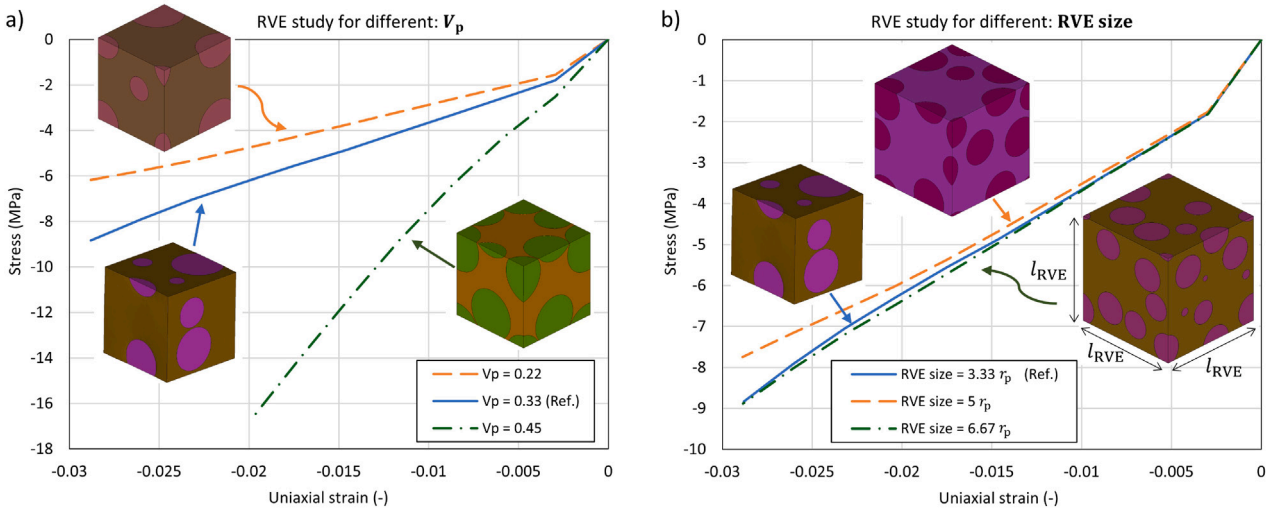

Fig. 5. Comparison of different microscale RVE configurations (for the anode RVE). (a) Different volume fraction of particles (V_p). (b) Different RVE sizes, where l_{RVE} and r_p refers to the RVE outer dimension and particle radius, respectively.

on the virtual response of the stack) in tension are listed in Fig. 6d and summarized in Table 4, with hardening behavior in compression and shear based on results in Fig. 6c. Hence, the hardening curves for the jellyroll are based on the simulated data from the RVE load cases and are imported directly as *Load curves*. Finally, the simulation model and the test specimen are shown in Fig. 6d for comparison.

Utilizing the estimated material model parameters for the jellyroll from the virtual testing, the mechanical impact load case shown in Fig. 7a is simulated. The simulation is performed using the explicit solver in LS-Dyna with the penalty-based global contact formulation [45]. Both the static and dynamic friction are set to 0.15, and a time step scale factor of 0.9 is used to scale the critical time step estimated by the software (based on the smallest element size and material wave speed). For the explicit solver, the time step is controlled by the software guaranteeing numerical stability. In addition, mechanical impact testing was performed on the corresponding jellyroll test specimen (Fig. 7a). The jellyroll was tested in dry conditions (comparable with the utilized experimental data from literature) with a load application speed of 1 mm/min (quasi-static). In Fig. 7b, the force versus displacement of the impactor during the simulation and experiment are shown. The simulation model are in close agreement for small strains (in accordance with the assumption of small strains for the utilized constitutive models), while a slight deviation is observed for larger compression.

Table 4
Summary of model parameters used as input for the mesoscale RVE and the impact simulation model for the small scale jellyroll sample. Output from the RVE simulation is the average stress–strain response of the stack in the different directions and the force–displacement (of the impactor) from the impact simulation. Parameters marked as "Pre-calibrated" have been estimated in the (*initialization*) step based on experimental data, "Load curves" are imported experimental data (Exp), or simulated data from the RVE load cases (Sim), directly added as tabular values, and "Fixed" are fixed values.

Input	Parameter	Definition	Data type	Output
Geometry: Mesoscale RVE	RVE side length	$l_{\text{RVE}} = 227$ μm	Fixed	Stress–strain response
	Thickness of layers	See Table 5	Fixed	
	Solid elements (8 nodal hexahedral)	1872	Fixed	
	Approximate element size	18 μm	Fixed	
Material: Anode	Elastic modulus (tension)	$E_{\text{ano}} = 4.19$ GPa	Pre-calibrated	
	Poisson's ratio	$\nu_{\text{ano}} = 0.01$	Fixed	
	Tensile stress cutoff	$\sigma^T_{\text{ano}} = 28$ MPa	Pre-calibrated	
	Hardening curve	$p_{y,\text{ano}}(\varepsilon_v)$, Fig. 6b	Load curve (Exp)	
Material: Cathode	Elastic modulus (tension)	$E_{\text{cat}} = 4.83$ GPa	Pre-calibrated	
	Poisson's ratio	$\nu_{\text{cat}} = 0.01$	Fixed	
	Tensile stress cutoff	$\sigma^T_{\text{cat}} = 26$ MPa	Pre-calibrated	
	Hardening curve	$p_{y,\text{cat}}(\varepsilon_v)$, Fig. 6b	Load curve (Exp)	
Material: Separator	Elastic modulus (tension)	$E_{\text{sep}} = 0.93$ GPa	Pre-calibrated	
	Poisson's ratio	$\nu_{\text{sep}} = 0.01$	Fixed	
	Tensile stress cutoff	$\sigma^T_{\text{sep}} = 100$ MPa	Pre-calibrated	
	Hardening curve	$p_{y,\text{sep}}(\varepsilon_v)$, Fig. 6b	Load curve (Exp)	
Material: Cu collector	Elastic modulus	$E_{\text{Cu}} = 57.8$ GPa	Pre-calibrated	
	Poisson's ratio	$\nu_{\text{Cu}} = 0.3$	Fixed	
	Yield stress	$\sigma_{\text{Cu}} = 122$ MPa	Pre-calibrated	
	Hardening curve	$\sigma_{y,\text{Cu}}(\bar{\varepsilon}^p_n)$, Fig. 6b	Load curve (Exp)	
Material: Al collector	Elastic modulus	$E_{\text{Al}} = 49$ GPa	Pre-calibrated	
	Poisson's ratio	$\nu_{\text{Al}} = 0.3$	Fixed	
	Yield stress	$\sigma_{\text{Al}} = 94$ MPa	Pre-calibrated	
	Hardening curve	$\sigma_{y,\text{Al}}(\bar{\varepsilon}^p_n)$, Fig. 6b	Load curve (Exp)	
Geometry: Jellyroll impact	Length/Width jellyroll	70 mm	Fixed	Force–displacement
	Thickness of sample	1.82 mm	Fixed	
	Solid elements (8 nodal hexahedral)	41 067	Fixed	
	Shell elements (4/3 nodal quad/tri)	601	Fixed	
	Approximate element size	0.6 mm	Fixed	
Material: Jellyroll	Elastic modulus x-dir.	$E_{\text{xx}} = 0.75$ GPa	Based on RVE	
	Elastic modulus y/z-dir.	$E_{\text{yy}} = E_{\text{zz}} = 1.77$ GPa	Based on RVE	
	Elastic modulus xy/xz-dir.	$E_{\text{xy}} = E_{\text{xz}} = 0.61$ GPa	Based on RVE	
	Elastic modulus yz-dir.	$E_{\text{yz}} = 1.22$ GPa	Based on RVE	
	Poisson's ratios	$\nu_{\text{xx}} = \nu_{\text{yy}} = \nu_{\text{xy}} = \nu_{\text{yz}} = 0.01$	Fixed	
	Hardening curve x-dir.	$p_{y,\text{xx}}(\varepsilon_v)$, Fig. 6c	Load curve (Sim)	
	Hardening curve y/z-dir.	$p_{y,\text{yy}}(\varepsilon_v) = p_{y,\text{zz}}(\varepsilon_v)$, Fig. 6c	Load curve (Sim)	
	Hardening curve xy/xz-dir.	$p_{y,\text{xy}}(\varepsilon_v) = p_{y,\text{xz}}(\varepsilon_v)$, Fig. 6c	Load curve (Sim)	
	Hardening curve yz-dir.	$p_{y,\text{yz}}(\varepsilon_v)$, Fig. 6c	Load curve (Sim)	

Table 5
Small scale jellyroll sample, geometric model parameters and material models used. Single-side coated electrodes. Thicknesses measured using a high precision thickness gauge. Notations: Nickel Manganese Cobalt-oxide (NMC), Polyethylene (PE).

Layer	Material	Thickness	Material model	Reference
Anode coating	Graphite	88 μm	Uncoupled crushable foam (*MAT_063)	[15]
Cathode coating	NMC	80 μm	Uncoupled crushable foam (*MAT_063)	[15]
Separator	PE	16 μm	Uncoupled crushable foam (*MAT_063)	[15]
Cu collector	Copper	11 μm	Piecewise linear plasticity (*MAT_024)	[15]
Al collector	Aluminium	16 μm	Piecewise linear plasticity (*MAT_024)	[15]

In Fig. 7c, the mean pressure at the middle and at the end of the loading scenario are shown. Additionally, the test sample after the experiment is shown for comparison. It is found that the observed pattern of the pressure field in the simulation is similar to the one observed in the experiment. The non-uniform pattern is assumed to be associated with the sample shape (being a square).

The measured diameter $d^{\text{E}}_{\text{imp}}$ of the impact pattern (illustrated in Fig. 7c), and the corresponding simulated measure $d^{\text{S}}_{\text{imp}}$, are found to be approximately 13.3 mm and 12.7 mm, respectively. Moreover, the eight distinct corners of the impact pattern, as well as the small circular hot-spot in the middle of the impact area, are clearly distinguishable (and have similar dimensions) in both the tested and simulated specimen. Hence, close quantitative agreement between the numerical prediction and the experimental results are found in terms of the mode of deformation. This means that the physics of the experiment is well captured in the simulation model, and that the model provides a physically sound base for further fine-tuning of model parameters.

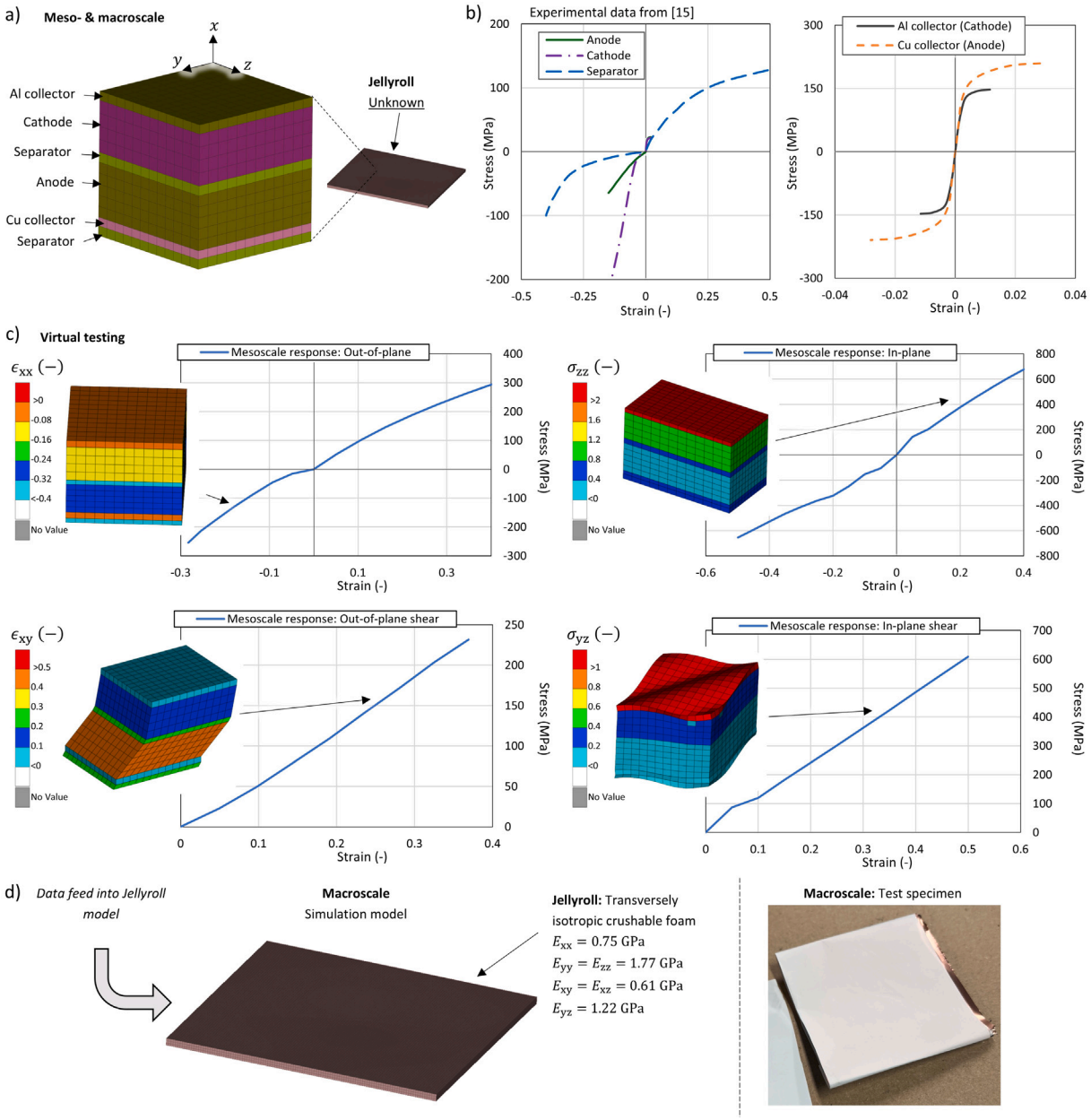

Fig. 6. Meso- and macroscale for small scale jellyroll sample. Design loop 2: Estimating effective properties of the jellyroll (note: single-side coated electrodes). (a) The unknown material response is the jellyroll. (b) Experimental data for the electrode layers from [15]. (c) Virtual testing. Plots showing the effective stress ($\bar{\sigma}$) versus the effective strain ($\bar{\varepsilon}$) for the different RVE load cases. (d) The simulation model for the jellyroll sample (and estimated model parameters in tension), and the corresponding test specimen.

4.2.2. *Prismatic battery cell testing*

For the final validation step, we utilize the same procedure as described for the small scale jellyroll sample but for the prismatic battery cell (including casing) shown in Fig. 8. The model parameters used as input for the mesoscale RVE model and the impact simulation model for the prismatic battery cell are provided in Table 6. The mesoscale RVE for the electrodes-separator stack for the prismatic cell is presented in Fig. 8a. This battery cell geometry corresponds to the one studied in the work by Purantagi [53]. The geometric model parameters and material models used are listed in Table 7. We note that the thickness of the individual layers are estimated (not exactly what is found in the tested battery cell) and normalized with respect to the total thickness of the RVE. For the virtual testing load cases the implicit solver in LS-Dyna is used, while the explicit solver (with global contact formulation) is used for the impact load case [45]. In Fig. 8b, the effective stress ($\bar{\sigma}$) versus the effective strain ($\bar{\varepsilon}$) is shown for the out-of-plane tension and compression. Based on the virtual testing, we again estimate the properties of the jellyrolls, which are summarized in Table 6 (results from virtual testing collected in Appendix A). The mechanical impact simulation model is shown in Fig. 8c–d. The aluminium casing is treated as a homogeneous material using the piecewise linear elasto-plastic constitutive model as shown in Fig. 8c (cf. [54]), and with normalized thicknesses listed in Table 7. The support and impactor are treated as rigid bodies (Fig. 8d). The graph in Fig. 8e shows the normalized force (exerted on the impactor) versus the displacement of the impactor for the simulation and the corresponding experimental data. The loading speed for the test is 1 mm/s, which motivates the assumption of quasi-static conditions. It should be noted that the experimental test is now performed on a active fully charged battery cell. The normalized cell voltage is included for illustrative purpose, indicating

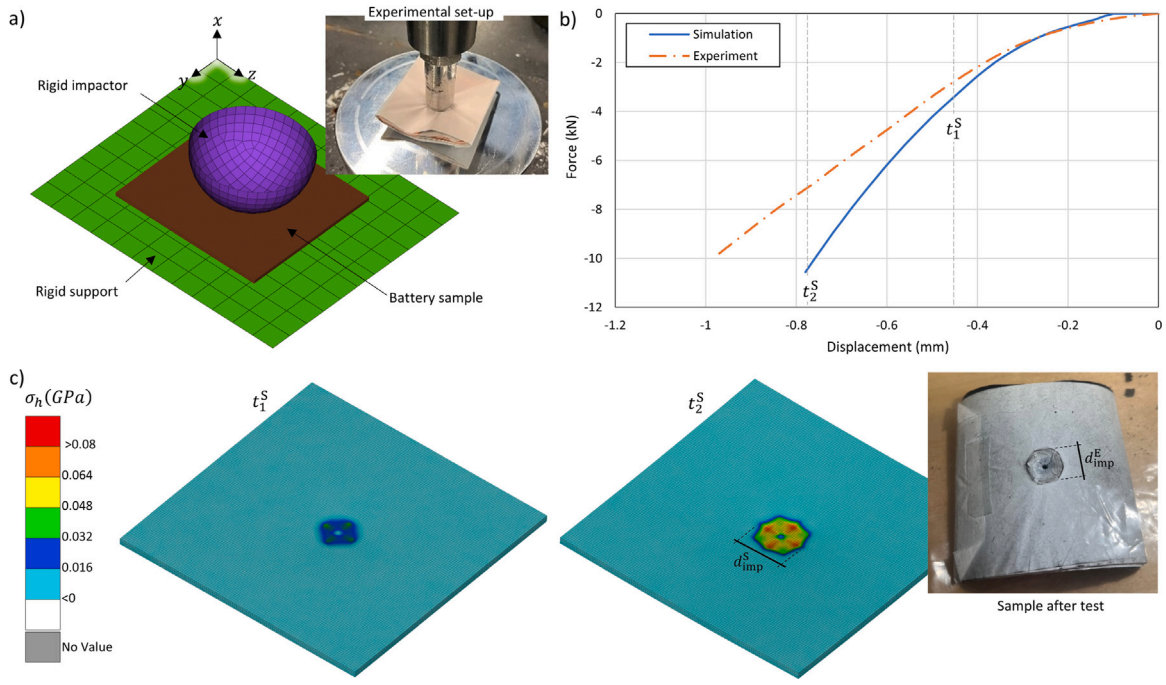

Fig. 7. Impact loading case for the small scale jellyroll specimen (quasi-static loading). (a) Model and experimental setup. (b) Force vs. displacement of the impactor for the simulation and experiment. (c) Mean pressure during the impact. Comparison between pressure field at the end of the simulation with sample after the impact test. Note: test performed on dry samples. The measured and simulated diameter of the impact pattern are denoted $d^{\mathrm{E}}_{\mathrm{imp}}$ and $d^{\mathrm{S}}_{\mathrm{imp}}$, respectively.

a distinct drop at high impact force and displacement (associated with ISC). It should be noted that the current simulation model does not include the electro-chemical problem. Due to the difference in time scales between mechanical failure and the thermal- and electrochemical processes, mechanical modeling alone is often sufficient to predict the onset of internal short circuits in early-stage safety assessments, cf. [34]. However, for future work considering operational conditions, the current modeling framework can serve as a base for populating and estimating the mechanical response of the various material phases inside the battery, prior to adding the relevant additional physics. It is worth noting that for the initial simulation (*Simulation Initial*), no additional calibration has been performed at this stage. The response of the jellyroll is solely based on the virtual response of the electrodes-separator stack RVE with calibrated material parameters in terms of the properties of the individual layers (at the mesoscale). The simulation and experimental results agree well for small strains, in agreement with the model assumptions (constitutive models based on small strain theory). The difference between the simulated and experimental results is assumed to be due to the various uncertainties and simplifications e.g., model simplifications (e.g. utilized material models and boundary conditions), test data on dry, non-active samples (i.e. not accounting for changes in stiffness associated with e.g. SOC [20]), etc. The main advantage of this model setup is however, that we can now study the influence of various material or geometrical parameters and features. Hence, the method provides a favorable initial guess to further calibration (optimization) steps, and the influence and importance of various factors can be assessed when evaluating the robustness and safety of different battery cells exposed to mechanical impact loading. To illustrate this we have included an example of a calibrated response of the jellyroll in Fig. 8e (*Simulation Calibrated*). In this calibration loop (corresponding to the *final calibration* step described in Section 3.4), the design parameters are limited to the hardening curve of the jellyroll in the out-of-plane direction ($p_{y,\mathrm{xx}}(\varepsilon_v)$) and only minor changes are allowed (compared to the initial guess from virtual testing). Additional information on the utilized design space for the calibration loop is provided in Appendix A. These parameters are selected because it is assumed that they are the most influential for the given loading scenario, in combination with the introduction of the liquid electrolyte and change in SOC. As can be seen, close agreement between numerical and experimental result are now obtained (as expected). It is worth noting, however, that there is a slight deviation between the calibrated response and the experimental data under high compression load. This difference is thought be, in particular, due to the fact that only the parameters representing the hardening curve in the out-of-plane direction for the jellyroll are included in the calibration loop. Hence, improved accuracy can be obtained by increasing the design space, including additional material parameters representing the remaining hardening curves (in the other directions) and elastic properties.

4.3. Comparing the computational run times

All simulations are conducted using LS-DYNA version 14.1.0 AVX2 with double precision, on a high-performance computing cluster. The implicit solver is used for the RVE load cases with default convergence criteria, while the explicit solver is used for the impact problems.[2] The estimated computational run times (or CPU times) for the different models are listed in Table 8 together with the solver type and number of elements. The run time here refers to the wall-clock time measured from the start of the solver execution until completion (excluding pre- and post-processing stages). The simulations were executed using 24 CPU cores (in parallel) with a total shared memory of approximately 4.1 GB allocated for Message Passing Interface communication.

From Table 8, it is clear that the simulation time varies significantly between the different models. For example, the run time for the macroscale impact model for the prismatic battery cell is approximately 34 times longer compared with the microscale RVE (reference model). For the calibration loops, the run time for the individual model is critical as is it has a large impact on the total solver time. This is due to

[2] For the explicit solver, the time step is determined by the software. For example, the actual time step used in the impact simulation of the prismatic battery cell was $4.86 \cdot 10^{-4}$ s with a maximum stable time step of $6.94 \cdot 10^{-4}$ s.

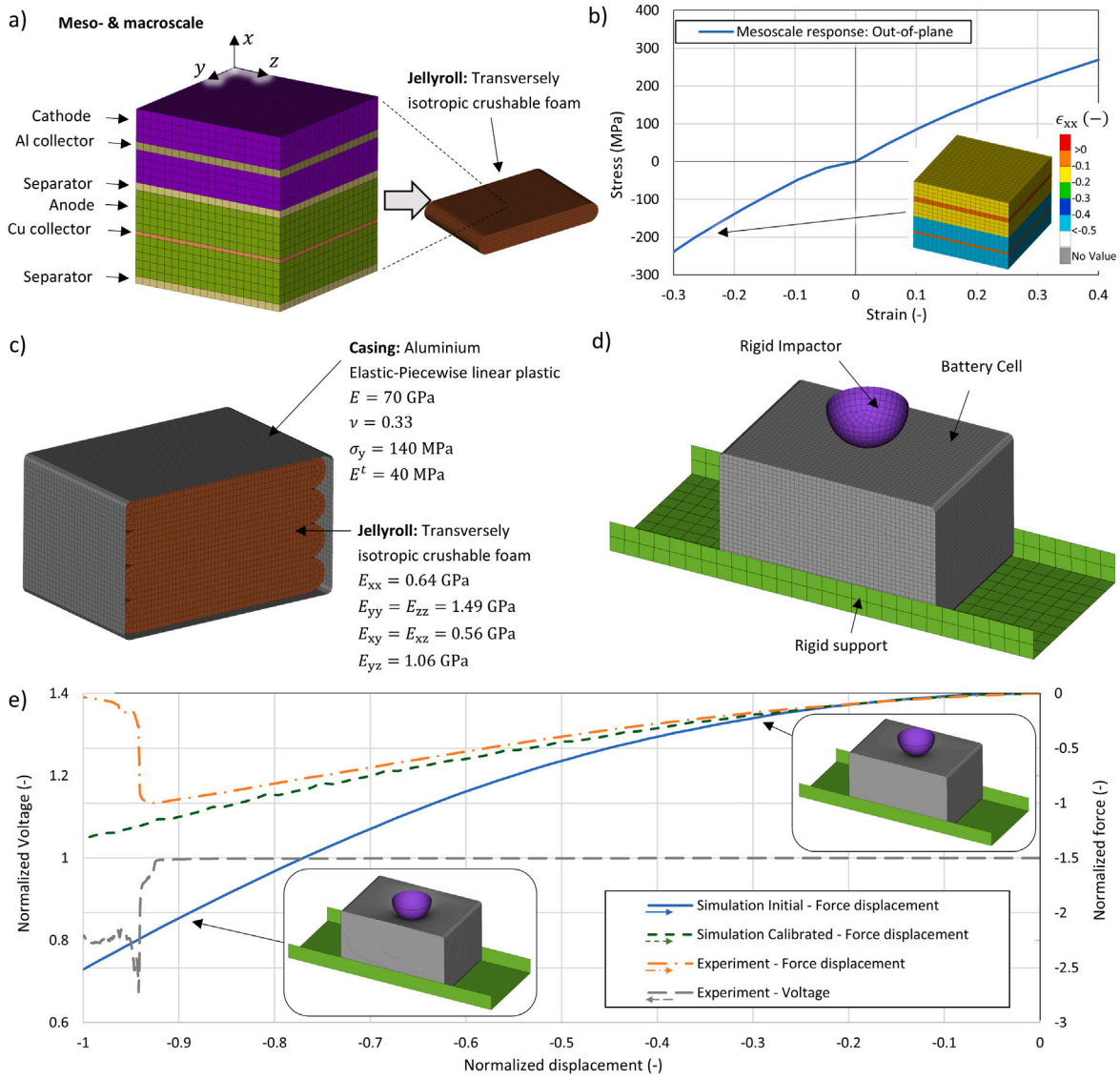

Fig. 8. Meso- and macroscale for prismatic battery cell. Design loop 2: Estimating effective properties of the jellyroll (note: double-side coated electrodes). (a) The unknown material response is the jellyroll. (b) Virtual testing. Plot showing the effective stress ($\bar{\sigma}$) versus the effective strain ($\bar{\varepsilon}$) for out-of-plane compression and tension. (c)–(d) The simulation model for the prismatic battery cell. (e) Normalized force vs. displacement of the impactor for the simulation and experiment. *Simulation Initial*: Initial guess from virtual testing. *Simulation Calibrated*: Hardening curve of the jellyroll in the out-of-plane direction calibrated. Note: Sample tested in operating conditions i.e. containing electrolyte and the cell was fully charged. The yield stress and tangential modulus for the casing are denoted σ_y and E^t, respectively.

the fact that the calibration loops are set to execute 15 simulations for each iteration, with a total of 10 iterations. To speed up this process, we executed the individual (15) simulations within each iteration in parallel (only possible with high-performance computing clusters). Finally, it should be noted that the computational cost depends strongly on e.g. the choice of solver type, integration scheme, number of elements, etc.

5. Conclusions and outlook to future work

In this work, a multiscale modeling framework for estimating the mechanical response of the material phases (at various length scales) in Li-ion batteries is presented.

Two design optimization loops for calibrating material model parameters are set up and performed. In the first design loop we back-calculate the material properties for the binder-conductive additive-electrolyte matrix of the anode and cathode electrodes, in terms of the selected constitutive model. In this work, we utilize the Crushable foam material model available in the LS-Dyna suite. The material properties are estimated by performing homogenization of microscale RVEs for the individual electrode layers, while utilizing experimental data for the effective response of the electrode layer and the electrode particles (available in literature). The numerical results reveal that the proposed design loop is able to retrieve the material model parameters for the matrix. Further, the results show that the estimated parameters are noticeably affected by the volume fraction of particles and the quality of the experimental data. These results can, e.g., be used to study residual stresses and strains due to particle swelling/contraction (at the microscale) potentially giving rise to delamination or debonding [55, 56].

In the second design loop we estimate the effective properties of the jellyroll by performing homogenization on RVEs of the electrodes-separator stack. Firstly, we study a small scale jellyroll sample and

Table 6
Summary of model parameters used as input for the mesoscale RVE and the impact simulation model for the prismatic battery cell. Output from RVE simulation is the average stress–strain response of the stack, and impact simulation is force–displacement. Parameters listed as "see Table 4" indicates values reused from the small-scale jellyroll sample, estimated in the (*initialization*) step. "Load curve (Sim)" denotes imported simulated data from the RVE load cases, directly added as tabular values, and "Fixed" are fixed values. "Load curve (Calibrated)" refers to parameters included as design variables in the *final calibration* loop. Figure S1 and information on calibration design space are found in Appendix A.

Input	Parameter	Definition	Data type	Output
Geometry: Mesoscale RVE	Side length (normalized)	$l_{RVE} = 1$	Fixed	Stress–strain response
	Thickness of layers	See Table 7	Fixed	
	Solid elements (8 nodal hexahedral)	8800	Fixed	
	Approximate element size	$\frac{\text{RVE thickness}}{20}$	Fixed	
Materials RVE:	Anode, cathode, separator, collectors	See Table 4		
Geometry: Prismatic impact	Number of jellyrolls	4	Fixed	Force–displacement
	Thickness of jellyroll	20 mm	Fixed	
	Solid elements (8 nodal hexahedral)	41 280	Fixed	
	Shell elements (4/3 nodal quad/tri)	8643	Fixed	
	Approximate element size	3 mm	Fixed	
Material: Jellyroll	Elastic modulus x-dir.	$E_{xx} = 0.64$ GPa	Based on RVE	
	Elastic modulus y/z-dir.	$E_{yy} = E_{zz} = 1.49$ GPa	Based on RVE	
	Elastic modulus xy/xz-dir.	$E_{xy} = E_{xz} = 0.56$ GPa	Based on RVE	
	Elastic modulus yz-dir.	$E_{yz} = 1.06$ GPa	Based on RVE	
	Poisson's ratios	$\nu_{xx} = \nu_{yy} = \nu_{xy} = \nu_{yz} = 0.01$	Fixed	
	Hardening curve x-dir.	$p_{y,xx}(\varepsilon_v)$, Fig. 8b	Load curve (Sim/Calibrated)	
	Hardening curve y/z-dir.	$p_{y,yy}(\varepsilon_v) = p_{y,zz}(\varepsilon_v)$, Fig. S1	Load curve (Sim)	
	Hardening curve xy/xz-dir.	$p_{y,xy}(\varepsilon_v) = p_{y,xz}(\varepsilon_v)$, Fig. S1	Load curve (Sim)	
	Hardening curve yz-dir.	$p_{y,yz}(\varepsilon_v)$, Fig. S1	Load curve (Sim)	
Material: Casing	Elastic modulus	$E = 70$ GPa	Fixed	
	Poisson's ratio	$\nu = 0.33$	Fixed	
	Yield stress	$\sigma_y = 140$ MPa	Fixed	
	Tangential modulus	$E^t = 40$ MPa	Fixed	

Table 7
Prismatic battery cell model parameters. Mesoscale RVE (stack level). Double-side coated electrodes. Notations: Nickel Manganese Cobalt-oxide (NMC), Polyethylene (PE). Note: The thicknesses of the individual layers and casing are estimated and normalized with respect to the total thickness of the RVE. Casing is divided in four sides: top (T), bottom (B), short-sides (SS) and long-sides (LS).

Layer	Material	Normalized thickness	Material model	Reference
Anode coating	Graphite	0.47	Uncoupled crushable foam (*MAT_063)	[15]
Cathode coating	NMC	0.38	Uncoupled crushable foam (*MAT_063)	[15]
Separator	PE	0.09	Uncoupled crushable foam (*MAT_063)	[15]
Cu collector	Copper	0.02	Piecewise linear plasticity (*MAT_024)	[15]
Al collector	Aluminium	0.04	Piecewise linear plasticity (*MAT_024)	[15]
Casing	Aluminium	9.6(T)/6.1(B)/3.5(SS)/2.9(LS)	Piecewise linear plasticity (*MAT_024)	–

Table 8
Simulation run times (or CPU times) for the different models. The implicit solver was used for the RVE load case while the explicit solver was used for the impact simulations. Run time here refers to the wall-clock time measured from the start of the solver execution until completion.

Length scale	Model	Solver	Nr. elements (Solid/Shell)	Run time (s)
Microscale	RVE (ref.)	Implicit	35 444/0	19
Microscale	RVE (RVE size = 5 r_p)	Implicit	236 440/0	61
Microscale	RVE (RVE size = 6.67 r_p)	Implicit	518 819/0	160
Mesoscale	RVE small scale jellyroll sample	Implicit	1872/0	10
Mesoscale	RVE prismatic battery cell	Implicit	8800/0	31
Macroscale	Impact small scale jellyroll sample	Explicit	41 067/601	72
Macroscale	Impact prismatic battery cell	Explicit	41 280/8643	649

perform a (quasi-static) mechanical impact loading scenario. The impact load case is simulated utilizing the effective properties of the jellyroll, retrieved via virtual testing. The simulation and experimental results are found to be in close agreement for small strains (in accordance with the assumption of small strains for the utilized constitutive models), while a slight deviation is observed for larger compression. These results demonstrate that the provided framework is well suited for estimating the effective response of the jellyroll, based on test- and geometric data for the electrodes-separator layout.

Finally, a prismatic battery cell (including casing) is studied utilizing the same procedure. The simulation and experimental results are (also for this case) found to be in close agreement for small strains while deviating for larger compression. One of the main advantages of this process, is that we can at this point run additional calibration loops or

sensitivity studies to fine-tune/calibrate model or material parameters, or identify the influence of various material or geometrical parameters and features. This enables us to study the importance of various factors when evaluating the robustness and safety of different battery cells exposed to mechanical impact loading. Moreover, the method provides a favorable initial guess to the final calibration (optimization) problem, limiting the design space and reducing the risk for ending up in local optima.

By connecting the length scales via a homogenization scheme, and calibrating the constitutive models, we foresee that the current framework will provide a foundation for exploring (mechanical) failure mechanisms at different length scales associated with internal short-circuit triggered by mechanical impact on battery cells (future work). In particular, by introducing a modeling scheme for mapping the stresses/strains from the macroscale "back" to the mesoscale, it will be possible to estimate the stress and strain state within the individual layers inside the battery cell (to compare with failure stresses or strains of the individual components), cf. [23]. We note that for EV application, such a study should be accompanied with the introduction of strain rate dependency in the constitutive model description (cf. [57]), additional loading scenarios, and should consider the involved (remaining) physical phenomena (cf. [21,43]). These tools will provide valuable information, enabling improved understanding of the involved failure mechanisms during mechanical impact, which may trigger unwanted short-circuit processes or electrochemical degradation. Furthermore, methods for generating more realistic microstructures (see e.g., [58–60]) for the microscale RVEs will be explored in future work. This is critical when attempting to resolve local stress fields within the electrode. It is also worth noting that the electrode particles are known to change volume as well as elastic properties with degree of lithiation [50]. Hence, the proposed calibration procedure allows for studying the effect of lithiation (or SOC) on the mechanical response of the electrodes as well as swelling effects. In terms of model fidelity, we also note that accounting for large deformations/strains (e.g., hyperelastic response, cf. Larsson et al. [61]) is a relevant next step. Finally, various parametric studies would be relevant to pursue to evaluate different material parameters, designs and concepts. By knowing the significance of the individual parameters relative to the effective response, it is possible to guide future experiments on e.g., what data that is most important to retrieve and its sensitivity to measurement errors, as well as guide the design of battery cells for improved robustness (impact resistance) and safety.

CRediT authorship contribution statement

David Carlstedt: Writing – original draft, Visualization, Validation, Supervision, Software, Project administration, Methodology, Investigation, Formal analysis, Data curation, Conceptualization. **Amit Chetry:** Writing – review & editing, Visualization, Software, Methodology, Formal analysis, Data curation, Conceptualization. **Carl Larsson:** Writing – review & editing, Methodology. **Ankeet Mohan Purantagi:** Writing – review & editing, Conceptualization. **Peter Gustavsson:** Writing – review & editing, Methodology, Data curation. **Fredrik Larsson:** Writing – review & editing, Supervision, Methodology, Funding acquisition, Conceptualization. **Leif E. Asp:** Writing – review & editing, Supervision, Methodology, Funding acquisition, Conceptualization.

Declaration of competing interest

The authors declare that they have no known competing financial interests or personal relationships that could have appeared to influence the work reported in this paper.

Acknowledgments

Fredrik Larsson, Leif E. Asp and Amit Chetry acknowledge funding from the Swedish research initiative COMPEL (competence and excellence for the electrification of the transport system), Sweden.

Appendix A. Supplementary data

Supplementary material related to this article can be found online at https://doi.org/10.1016/j.jpowsour.2025.238237.

Data availability

All data, except experimental test data from the prismatic cell impact testing, will be made available on request. The raw data from the prismatic cell testing is confidential.

References

[1] G. Kermani, E. Sahraei, Review: Characterization and modeling of the mechanical properties of lithium-ion batteries, Energies 10 (2017) http://dx.doi.org/10.3390/en10111730.
[2] B. Liu, Y. Jia, C. Yuan, L. Wang, X. Gao, S. Yin, J. Xu, Safety issues and mechanisms of lithium-ion battery cell upon mechanical abusive loading: A review, Energy Storage Mater. 24 (2020) 85–112, http://dx.doi.org/10.1016/j.ensm.2019.06.036.
[3] X. Duan, H. Wang, Y. Jia, L. Wang, B. Liu, J. Xu, A multiphysics understanding of internal short circuit mechanisms in lithium-ion batteries upon mechanical stress abuse, Energy Storage Mater. 45 (2022) 667–679, http://dx.doi.org/10.1016/j.ensm.2021.12.018.
[4] Y. Li, C. Wei, Y. Sheng, F. Jiao, K. Wu, Swelling force in lithium-ion power batteries, Ind. Eng. Chem. Res. 59 (2020) 12313–12318, http://dx.doi.org/10.1021/acs.iecr.0c01035.
[5] Y. Cao, H. Wang, B. Liu, J. Xu, Modeling, validation, and analysis of swelling behaviors of lithium-ion batteries, J. Energy Storage 74 (2023) 109499, http://dx.doi.org/10.1016/j.est.2023.109499.
[6] S. Sun, J. Xu, Safety behaviors and degradation mechanisms of aged batteries: A review, Energy Mater. Devices 2 (2024) 9370048, http://dx.doi.org/10.26599/EMD.2024.9370048.
[7] G. Zhang, X. Wei, X. Tang, J. Zhu, S. Chen, H. Dai, Internal short circuit mechanisms, experimental approaches and detection methods of lithium-ion batteries for electric vehicles: A review, Renew. Sustain. Energy Rev. 141 (2021) 110790, http://dx.doi.org/10.1016/j.rser.2021.110790.
[8] J. Zhu, T. Wierzbicki, W. Li, A review of safety-focused mechanical modeling of commercial lithium-ion batteries, J. Power Sources 378 (2018) 153–168, http://dx.doi.org/10.1016/j.jpowsour.2017.12.034.
[9] E. Sahraei, R. Hill, T. Wierzbicki, Calibration and finite element simulation of pouch lithium-ion batteries for mechanical integrity, J. Power Sources 201 (2012) 307–321, http://dx.doi.org/10.1016/j.jpowsour.2011.10.094.
[10] E. Sahraei, J. Campbell, T. Wierzbicki, Modeling and short circuit detection of 18650 Li-ion cells under mechanical abuse conditions, J. Power Sources 220 (2012) 360–372, http://dx.doi.org/10.1016/j.jpowsour.2012.07.057.
[11] T. Wierzbicki, E. Sahraei, Homogenized mechanical properties for the jellyroll of cylindrical lithium-ion cells, J. Power Sources 241 (2013) 467–476, http://dx.doi.org/10.1016/j.jpowsour.2013.04.135.
[12] L. Greve, C. Fehrenbach, Mechanical testing and macro-mechanical finite element simulation of the deformation, fracture, and short circuit initiation of cylindrical lithium ion battery cells, J. Power Sources 214 (2012) 377–385, http://dx.doi.org/10.1016/j.jpowsour.2012.04.055.
[13] C. Breitfuss, W. Sinz, F. Feist, G. Gstrein, B. Lichtenegger, C. Knauder, C. Ellersdorfer, J. Moser, H. Steffan, M. Stadler, P. Gollob, V. Hennige, A 'microscopic' structural mechanics FE model of a lithium-ion pouch cell for quasi-static load cases, SAE Int. J. Passeng. Cars - Mech. Syst. 6 (2013) 1044–1054, http://dx.doi.org/10.4271/2013-01-1519.
[14] J. Xu, B. Liu, X. Wang, D. Hu, Computational model of 18650 lithium-ion battery with coupled strain rate and SOC dependencies, Appl. Energy 172 (2016) 180–189, http://dx.doi.org/10.1016/j.apenergy.2016.03.108.
[15] M. Spielbauer, F. Peteler, A. Nemeth, J. Soellner, P. Berg, O. Bohlen, A. Jossen, An analysis of the current state and obstacles in discrete layered finite element simulation of crushing cylindrical lithium-ion cells, J. Energy Storage 72 (2023) 108029, http://dx.doi.org/10.1016/j.est.2023.108029.
[16] E. Sahraei, M.M. Keshavarzi, X. Zhang, B. Lai, Mechanical properties of prismatic Li-ion batteries—electrodes, cells, and stacks, J. Electrochem. Energy Convers. Storage 19 (2022) 041008, http://dx.doi.org/10.1115/1.4054823.
[17] P. Gupta, P. Gudmundson, Modeling of local electrode stresses and pressures in lithium-ion battery packs using three-dimensional homogenization, J. Power Sources 582 (2023) 233514, http://dx.doi.org/10.1016/j.jpowsour.2023.233514.
[18] S.H. Chung, T. Tancogne-Dejean, J. Zhu, H. Luo, T. Wierzbicki, Failure in lithium-ion batteries under transverse indentation loading, J. Power Sources 389 (2018) 148–159, http://dx.doi.org/10.1016/j.jpowsour.2018.04.003.
[19] M.M. Keshavarzi, M. Gilaki, E. Sahraei, Characterization of in-situ material properties of pouch lithium-ion batteries in tension from three-point bending tests, Int. J. Mech. Sci. 219 (2022) 107090, http://dx.doi.org/10.1016/j.ijmecsci.2022.107090.

[20] M. Gilaki, E. Sahraei, Modeling state-of-charge dependent mechanical response of lithium-ion batteries with volume expansion, Energy Rep. 12 (2024) 3607–3619, http://dx.doi.org/10.1016/j.egyr.2024.09.041.
[21] A. Mallarapu, S.-Y. Park, J. Lim, S.B. Han, S.M. Lee, B.-H. Choi, Y. Han, N. Sunderlin, S. Santhanagopalan, Numerical and experimental analysis of mechanically induced failure in electric vehicle battery modules, J. Power Sources 645 (2025) 237245, http://dx.doi.org/10.1016/j.jpowsour.2025.237245.
[22] S.R. Shinde, Y. Song, E. Sahraei, Modeling electric vehicle's battery module using computational homogenization approach, Int. J. Energy Res. 2023 (1) (2023) 9210078, http://dx.doi.org/10.1155/2023/9210078.
[23] Y. Song, M. Bulla, H. Patanwala, E. Sahraei, Validation of sahraei failure criterion on cylindrical and pouch lithium-ion battery cells, J. Energy Storage 94 (2024) 112371, http://dx.doi.org/10.1016/j.est.2024.112371.
[24] B. Rui, S. Sun, X. Tan, C.M. Chak, L. Ma, J. Xu, Mechanical abuse and safety in sodium-ion batteries, J. Mater. Chem. A (2025) http://dx.doi.org/10.1039/D5TA00624D.
[25] S. Kalnaus, H. Wang, T.R. Watkins, S. Simunovic, A. Sengupta, Features of mechanical behavior of EV battery modules under high deformation rate, Extrem. Mech. Lett. 32 (2019) 100550, http://dx.doi.org/10.1016/j.eml.2019.100550.
[26] M. Sprenger, N. Dölle, F. Schauwecker, M. Raffler, C. Ellersdorfer, W. Sinz, Multiscale analysis and safety assessment of fresh and electrical aged lithium ion pouch cells focusing on mechanical behavior, Energies 15 (2022) http://dx.doi.org/10.3390/en15030847.
[27] Y. Jia, X. Gao, L. Ma, J. Xu, Comprehensive battery safety risk evaluation: Aged cells versus fresh cells upon mechanical abusive loadings, Adv. Energy Mater. 13 (24) (2023) 2300368, http://dx.doi.org/10.1002/aenm.202300368.
[28] J. Cannarella, X. Liu, C.Z. Leng, P.D. Sinko, G.Y. Gor, C.B. Arnold, Mechanical properties of a battery separator under compression and tension, J. Electrochem. Soc. 161 (2014) http://dx.doi.org/10.1149/2.0191411jes.
[29] P. Gupta, M. Streb, A. Siddiqui, M. Klett, G. Lindbergh, P. Gudmundson, Layer-resolved mechanical degradation of a Ni-rich positive electrode, Batteries 9 (2023) http://dx.doi.org/10.3390/batteries9120575.
[30] A.H.S. Iyer, P. Gupta, P. Gudmundson, A. Kulachenko, Measuring microscale mechanical properties of pvdf binder phase and the binder-particle interface using micromechanical testing, Mater. Sci. Eng.: A 881 (2023) 145352, http://dx.doi.org/10.1016/j.msea.2023.145352.
[31] J. Zhu, Standardizing mechanical tests on Li-ion batteries to develop a useful cell-level model under extreme mechanical loads, J. Energy Storage 65 (2023) 107320, http://dx.doi.org/10.1016/j.est.2023.107320.
[32] Z. Pan, W. Li, Y. Xia, Experiments and 3D detailed modeling for a pouch battery cell under impact loading, J. Energy Storage 27 (2020) 101016, http://dx.doi.org/10.1016/j.est.2019.101016.
[33] S.S. Kulkarni, F. Vysoudil, T. Vietor, Evaluation of modelling and simulation strategies to investigate the mechanical integrity of a battery cell using finite element methods, Energies 14 (2021) http://dx.doi.org/10.3390/en14112976.
[34] E. Sahraei, E. Bosco, B. Dixon, B. Lai, Microscale failure mechanisms leading to internal short circuit in Li-ion batteries under complex loading scenarios, J. Power Sources 319 (2016) 56–65, http://dx.doi.org/10.1016/j.jpowsour.2016.04.005.
[35] G. Kermani, M. Keshavarzi, E. Sahraei, Deformation of lithium-ion batteries under axial loading: Analytical model and representative volume element, Energy Rep. 7 (2021) 2849–2861, http://dx.doi.org/10.1016/j.egyr.2021.05.015.
[36] P. Gupta, P. Gudmundson, A multi-scale model for simulation of electrochemically induced stresses on scales of active particles, electrode layers, and battery level in lithium-ion batteries, J. Power Sources 511 (2021) 230465, http://dx.doi.org/10.1016/j.jpowsour.2021.230465.
[37] J.M. Foster, Y. Hahn, H. Patanwala, V. Oancea, E. Sahraei, Mechanical deformation in lithium-ion battery electrodes: Modeling and experiment, J. Electrochem. Energy Convers. Storage 22 (2024) 011012, http://dx.doi.org/10.1115/1.4065534.
[38] I.B. Üçel, P. Gudmundson, A statistical RVE model for effective mechanical properties and contact forces in lithium-ion porous electrodes, Int. J. Solids Struct. 244–245 (2022) 111602, http://dx.doi.org/10.1016/j.ijsolstr.2022.111602.
[39] P. Gudmundson, P.-L. Larsson, An analytic model for effective mechanical properties and local contact stresses in lithium-ion porous electrodes, Extrem. Mech. Lett. 42 (2021) 101067, http://dx.doi.org/10.1016/j.eml.2020.101067.
[40] A.P. Roberts, E.J. Garboczi, Elastic properties of model porous ceramics, J. Am. Ceram. Soc. 83 (2000) 3041–3048, http://dx.doi.org/10.1111/j.1151-2916.2000.tb01680.x.
[41] A. Schmid, A. Pasquale, C. Ellersdorfer, M. Raffler, V. Champaney, M. Ziane, F. Chinesta, F. Feist, Mechanical Characterization of Li-ion Cells and the Calibration of Numerical Models Using Proper Generalized Decomposition, in: Proceedings of the ASME International Mechanical Engineering Congress and Exposition, 7: Energy, 2023, V007T08A046, http://dx.doi.org/10.1115/IMECE2023-113228.
[42] R. Li, W. Li, A. Singh, D. Ren, Z. Hou, M. Ouyang, Effect of external pressure and internal stress on battery performance and lifespan, Energy Storage Mater. 52 (2022) 395–429, http://dx.doi.org/10.1016/j.ensm.2022.07.034.
[43] D. Carlstedt, K. Runesson, F. Larsson, L.E. Asp, On the coupled thermo-electro-chemo-mechanical performance of structural batteries with emphasis on thermal effects, Eur. J. Mech. A Solids 94 (2022) 104586, http://dx.doi.org/10.1016/j.euromechsol.2022.104586.
[44] C.R. Siviour, J.L. Jordan, High strain rate mechanics of polymers: A review, J. Dyn. Behav. Mater. 2 (2016) 15–32, http://dx.doi.org/10.1007/s40870-016-0052-8.
[45] Ansys, LS-DYNA theory manual, Livermore Softw. Technol. Corp. Version R14 (2023) URL: https://ftp.lstc.com/anonymous/outgoing/web/ls-dyna_manuals/R14/LS-DYNA_Manual_Theory_R14.pdf.
[46] T. Borrvall, A heuristic attempt to reduce transverse shear locking in fully integrated hexahedra with poor aspect ratio, in: 7th European LS-DYNA Conference, Salzburg, Austria, 2009.
[47] T.I. Zohdi, P. Wriggers, An Introduction to Computational Micromechanics, Springer Science & Business Media, 2008.
[48] Ansys, LS-DYNA keyword user's manual, volume i, Livermore Softw. Technol. Corp. Version R14 (2023).
[49] Ansys, LS-DYNA keyword user's manual, volume II: Material models, Livermore Softw. Technol. Corp. Version R14 (2023).
[50] Y. Qi, L.G. Hector, C. James, K.J. Kim, Lithium concentration dependent elastic properties of battery electrode materials from first principles calculations, J. Electrochem. Soc. 161 (2014) F3010–F3018.
[51] S. Nielen, A. Basudhar, W. Roux, K. Liebold, T. Eggleston, T. Goel, K. Craig, LS-OPT user's manual, a design optimization and probabilistic analysis tool for the engineering analyst, Livermore Softw. Technol. Corp. Version 7.0 (2020) URL: https://www.lsoptsupport.com/.
[52] Y. Ji, X. Chen, T. Wang, H. Ji, Y. Zhang, Q. Yuan, L. Li, Coupled effects of charge–discharge cycles and rates on the mechanical behavior of electrodes in lithium–ion batteries, J. Energy Storage 30 (2020) 101577, http://dx.doi.org/10.1016/j.est.2020.101577.
[53] A.M. Purantagi, Predicting Short Circuit of Li-ion Battery Cells During Mechanical Abuse Master thesis, Chalmers University of Technology, 2024, URL: http://hdl.handle.net/20.500.12380/308741.
[54] T. Tancogne-Dejean, C.C. Roth, V. Grolleau, T. Beerli, D. Mohr, Using miniature experiments to reveal strength gradients in battery casings, Int. J. Mech. Sci. 275 (2024) 109253, http://dx.doi.org/10.1016/j.ijmecsci.2024.109253.
[55] R. Xu, Y. Yang, F. Yin, P. Liu, P. Cloetens, Y. Liu, F. Lin, K. Zhao, Heterogeneous damage in Li-ion batteries: Experimental analysis and theoretical modeling, J. Mech. Phys. Solids 129 (2019) 160–183, http://dx.doi.org/10.1016/j.jmps.2019.05.003.
[56] N. Iqbal, Y. Ali, S. Lee, Debonding mechanisms at the particle-binder interface in the Li-ion battery electrode, J. Electrochem. Soc. 167 (2020) 060515, http://dx.doi.org/10.1149/1945-7111/ab8479.
[57] T. Tancogne-Dejean, V. Grolleau, D. Mohr, Strain rate dependent plasticity of lithium-ion pouch cells: Experiments and simulations, Int. J. Impact Eng. 159 (2022) 104048, http://dx.doi.org/10.1016/j.ijimpeng.2021.104048.
[58] D.R. Rollin, F. Larsson, K. Runesson, R. Jänicke, Upscaling of chemo-mechanical properties of battery electrode material, Int. J. Solids Struct. 281 (2023) 112405, http://dx.doi.org/10.1016/j.ijsolstr.2023.112405.
[59] V. Nagda, A. Kulachenko, S.B. Lindström, Image-based 3D characterization and reconstruction of heterogeneous battery electrode microstructure, Comput. Mater. Sci. 223 (2023) 112139, http://dx.doi.org/10.1016/j.commatsci.2023.112139.
[60] F.L.E. Usseglio-Viretta, P. Patel, E. Bernhardt, A. Mistry, P.P. Mukherjee, J. Allen, S.J. Cooper, J. Laurencin, K. Smith, MATBOX: An open-source microstructure analysis toolbox for microstructure generation, segmentation, characterization, visualization, correlation, and meshing, SoftwareX 17 (2022) 100915, http://dx.doi.org/10.1016/j.softx.2021.100915.
[61] C. Larsson, F. Larsson, J. Xu, K. Runesson, L.E. Asp, Effects of lithium insertion induced swelling of a structural battery negative electrode, Compos. Sci. Technol. 244 (2023) 110299, http://dx.doi.org/10.1016/j.compscitech.2023.110299.